UNIVERSIDAD DE LOS ANDES
FACULTAD DE INGENIERÍA Y
CIENCIAS APLICADAS

A NOVEL FLUID DYNAMIC STUDY OF THE GAS-LIQUID FLOWS IN BIOTRICKLING FILTERS THROUGH CFD SIMULATIONS AND DIGITAL IMAGING TECHNIQUES

FELIPE ANTONIO CARREÑO LÓPEZ

THESIS PRESENTED IN PARTIAL FULFILLMENT OF THE REQUIREMENTS
DOCTORADO EN CIENCIAS DE LA INGENIERIA

ADVISOR: Dr. PATRICIO MORENO CASAS

Dr. ALBERTO VERGARA FERNÁNDEZ

SANTIAGO, 2022

Dedicated to Enrique Guillermo López Acevedo.

Daría lo que fuera por tenerte a mi lado en este momento.

ABSTRACT

Daily, tons of volatile organic compounds (VOCs) which negatively affect the environment and human health are emitted into the atmosphere from anthropogenic and natural sources. Biotrickling filtration (BTF) is becoming one of the most promising treatment technologies for odor control. Within the last decades, the treatment of pollutants have been studied, and diverse numerical models for predicting the mass transfer have been intensively developed. However, the current state of the art is mainly based on using the two-film, penetration, and surface renewal theories which do not account for local variations of the fluid velocities, physical properties, or flow regimes. To account for variations on the local physical processes, a detail description of porous media, the multiphase fluid dynamics, and the biomass film is required. This work investigates and extends a three-dimensional computational fluid dynamic (CFD) model coupled with computerized tomography (CT) with the novel incorporation of a contrast agent as a first attempt to assess the local biofilm formation inside a realistic porous structure used in biotrickling filtration of VOCs. The validation of these models was accomplished in terms of the gas and liquid phase residence time distribution (RTD), and the volumetric mass transfer coefficient. The gas phase RTD was obtained using a novel methodology based low cost MOx sensor; the liquid phase RTD was obtained from a methylene blue pulse method, while the mass transfer characterization was carried out by using the sulphite method. Finally, the column was operated for the treatment of toluene vapours and a contrast agent was added after reaching the steady state in order to obtain a 3D description of the local biofilm formation. These results were used to validate the CFD-CT models. The mean RTD and the normalized variance estimated in the simulation were 43.709 s and 0.326, respectively. Compared with the experimental results, a relative difference of 4.167% for the mean RTD and 32.515% for the normalized variance were found. The computed surface area was available for biodegradation was 0.366 m^2. This work results in a validated gas RTD model, whereas for the liquid RTD and mass transfer coefficient the proposed approaches seem promising but requires additional computational resources to assess the steady state behavior. This methodology demonstrated the feasibility to obtain the local biofilm formation but additional imaging procedures are required to reconstruct the closed manifold geometry to use this image as a computational mesh.

RESUMEN

Diariamente, enormes cantidades de compuestos orgánicos volátiles (COVs) son emitidos a la atmósfera tanto de fuente naturales como antropogénicas. La biofiltración de lecho

escurrido se ha transformado en una de las tecnologías más prometedoras para el control de olores. En las últimas décadas, el tratamiento de contaminantes gaseoso ha sido estudiado, y diversos modelos numéricos que buscan predecir la transferencia de masa han sido desarrollados. Sin embargo, el estado del arte acual se basa principalmente en el uso de las teorías de la capa límite, de penetración y renovación de superficie, las que no consideran la variación de las velocidades del fluido, propiedades físicas, o régimen de flujo en su estimación. Para tener en cuenta las variaciones en los procesos físicos locales, se requiere una descripción detallada de los medios porosos, la dinámica de fluidos multifásicos y la película de biomasa. Este trabajo investiga y amplía un modelo tridimensional de dinámica de fluidos computacional (DFC) acoplado con tomografía computarizada (TC) con la incorporación novedosa de un agente de contraste como un primer intento de evaluar la formación de biopelícula local dentro de una estructura porosa realista utilizada en biofiltración. La validación se logró en términos de la distribución del tiempo de residencia (DTR) de la fase gaseosa y líquida, y el coeficiente de transferencia de masa volumétrica. La DTR de la fase gaseosa se obtuvo utilizando una metodología novedosa basada en un sensor de MOx de bajo costo; la DTR en fase líquida se obtuvo mediante el método de pulso de azul de metileno, mientras que la caracterización de la transferencia de masa se realizó mediante el método del sulfito. Estos resultados se utilizaron para validar los modelos DFC-TC. El RTD medio y la varianza normalizada estimada en la simulación fueron 43,709 s y 0,326, respectivamente. En comparación con los resultados experimentales, se encontró una diferencia relativa de 4,167% para la RTD media y 32,515% para la varianza normalizada. Finalmente, la columna se operó para el tratamiento de tolueno y se añadió un agente de contraste después de alcanzar el estado estacionario para obtener una descripción 3D de la formación de biopelícula local, donde el área de superficie computada disponible para la biodegradación fue de 0,366 m2. Este trabajo da como resultado un modelo de RTD de gas validado, mientras que para el RTD de líquido y el coeficiente de transferencia de masa los enfoques propuestos parecen prometedores pero requieren recursos computacionales adicionales para evaluar el comportamiento de estado estacionario.

ACKNOWLEDGMENTS

First, I would like to thank my supervisors, Dr. Patricio Moreno, Dr. Alberto Vergara, and Dr. Raúl Muñoz, for guiding my research and supporting me throughout this pandemic Ph.D. journey. Thank you, Alberto and Raúl, for always being there for me and teaching me how

to be a great leader. Thank you, Patricio, for believing in me before I believed in myself and being my mental health support during this challenging journey.

Thanks to all the current and previous members of the G-Tech group lab for always supporting me. I want to thank Dr. Felipe Scott and Dr. Sichem Guerrero for helping me all these years; both are great inspirations. Special thanks to my dear friends Valentina Camilli and Luz Yañez; I will always be there for you. Thanks to the VOC and Microalgae group for being my pandemic family in Spain. Special thanks to Dr. José Sierra for being my second tutor in Spain; thank you for everything you taught me. Additionally, I would like to kindly thank Sandra Gutierrez from Clínica Universidad de Los Andes (Chile) for her help obtaining the CT-3D images.

The present work has been sponsored by CONICYT – Chile (National Commission for Scientific and Technological Research) (Fondecyt 1195021) and the Regional Government of Castilla y León, and the European FEDER Program (CLU 2017-09 and UIC 315). "Apoyo a la Formación de Redes Internacionales entre Centros de Investigación REDES190137", CONICYT-PCI. National Agency for Research and Development (ANID) / Scholarship Program / DOCTORADO NACIONAL / 2021 / 23220286.

Thanks to Galia Cooper, the first teacher who believed in me in high school. Without you, I would never ever thought about studying engineering. Thanks to Hector Pinto (RIP) for teaching me that chemistry is love. Thanks to my family and friends who encouraged me and supported me all these years. Especially to my mother, Angela, my two other mothers, Camila and Jeannette, and my partner Elisa Rojas; Thank you all for your patience and for loving me; I love you all so much.

Finally, I would thank my grandfather, Enrique, for everything. The world is boring without you, but I will try my best to make it better.

CONTENTS

LIST OF TABLES

LIST OF FIGURES

Figure 4. MOx sensor response time constant determination. (A) Ideal sensor response over a step stimulus under a steady state. The rise phase is the time range between the first stimulus and the maximum signal measurement. The decay phase corresponds to the time between the maximum measurement and the total time recovery of the signal. (B) Schematic

1 INTRODUCTION

Daily, tons of volatile organic compounds (VOCs) are emitted into the atmosphere from anthropogenic and natural sources (Koppmann, 2007). VOCs are a class of chemicals that easily become vapors or gases (vapor pressure ≥0.01 kPa at 20 °C) and are emitted into the atmosphere from natural sources in marine and terrestrial environments (Guenther et al., 1995; Kennes & Veiga, 2013), negatively affecting the environment and human health (Kennes & Veiga, 2001).

The United States Environmental Protection Agency (U.S EPA) classified some VOCs such as acrolein, acrylamide, vinyl chloride, ethylene oxide, (ethyl)benzene, carbon disulfide,

propylene oxide, styrene, tetrachloroethylene, toluene, trichloroethylene and xylene as hazardous air pollutants (US EPA, 2022) as they can adversely affect the health of humans and animals, in outdoors or indoors. In addition, the World Health Organization (WHO) also estimates that more than six million deaths are deported annually due to combined household and ambient air pollution (WHO, 2018). This pollution causes diverse adverse health effects, especially mortality and morbidity, as several VOCs are mutagenic, genotoxic, neurotoxic, and carcinogenic. Additionally, they are precursors of the formation of photochemical smog, ozone, and respirable suspended particulates in the atmosphere, contributing to the destruction of forests and ecosystems (Yang et al., 2010).

Various technologies have recently been developed to improve the air quality caused by VOCs and odorous gases. In general, these technologies can be classified into three categories: physical technologies, which mainly include condensation, adsorption, and absorption; chemical technologies, which usually include thermal oxidation, catalytic oxidation, and ozonation; and biological technologies, which include conventional biofiltration (BF), bio-scrubbers, biotrickling filtration (BTF) and other bioreactor configurations (Kennes & Veiga, 2013). Despite the effectiveness of physical-chemical methods in destroying and removing these gases, their main disadvantages are the high costs and the secondary pollution involved (Wu et al., 2018a). For some applications of physical-chemical techniques, waste gas concentration should be relatively high; otherwise, economic benefits are unachievable (Khan & Kr. Ghoshal, 2000).

Biotechnologies are currently recognized as the best available methods for treating low and moderate concentrations of waste gases (usually < 3 g m^{-3}) containing odorous pollutants and VOCs, where 99% odour reduction can be achieved for some contaminants (Groenestijn & Kraakman, 2005). Additionally, they are cost-effective and environment-friendly compared with other physical and chemical technologies (Revah & Morgan-Sagastume, 2005; Shareefdeen & Singh, 2005). From these technologies, biofiltration of VOCs is a complex combination of different physicochemical and biological phenomena in which the gaseous pollutant that flows through a packed bed is transferred from the gas phase into an immobilized biofilm attached to the packing material to be incorporated into their metabolism as a source of carbon and energy (Cheng et al., 2016).

In recent years, BTF technology is becoming one of the most promising treatment technologies for odour control (Cox & Deshusses, 2001). In BTF configurations, an aqueous solution is continuously trickled over the packing media, which is usually inert (inorganic), to provide water and essential nutrients to the microbial community, which must be previously inoculated from an external source (Wu et al., 2018a). In addition, this configuration has the advantage of operating under lower pressure drops during long-term operations and requires low operational and capital costs (Lebrero et al., 2012). However, the two main limitations in the process are the excess biomass accumulation and the low mass transfer rate in the presence of hydrophobic pollutants. Thus, parameters such as the reactor configuration, the physical properties of the packing material, the mass transfer, the operational conditions, and the microorganism's affinity to the pollutant are critical and significantly affect the removal of contaminants.

In the design of BTFs, it is crucial to understand which phenomena, such as the mass transfer and biodegradation kinetic limitations, limit the operation (Kraakman et al., 2011). Research on mass transfer limitation has been conducted by quantifying the mass transfer coefficient between the gas-liquid interface (Alonso et al., 1998b; Baltzis et al., 2001; Kim & Deshusses, 2008a), the gas-biofilm interface (Vergara-Fernandez et al., 2020) and the liquid-biofilm interface (Devinny & Ramesh, 2005; Kim & Deshusses, 2003). However, this mass transfer quantification is usually estimated using correlations obtained from gas absorption or distillation that have been brought under different operational conditions from those used in biofiltration systems, which results in overestimations (Kim & Deshusses, 2008a). Additionally, Wang et al. (2005) concluded that these correlations do not include insight from the fluid dynamics ongoing inside the packed bed; hence new correlations that consider the complex fluid dynamics behavior must be implemented.

The residence time distribution (RTD) is a well-known methodology employed to experimentally characterize the fluid dynamic behavior in multiple systems involving flows (Aparicio-Mauricio et al., 2020; Gao et al., 2020; Prades et al., 2017). Furthermore, this technique allows the analysis of flow non-idealities in reactors and can contribute to understanding fluid-dynamics effects such as channelling and flow maldistribution (Gunjal et al., 2003). However, the RTD analyses and the mass transfer coefficient estimation must be carried out *in situ* to obtain a diagnosis specific to the already operating reactor. Therefore,

they cannot be applied to predict the flow behavior or the mass transfer coefficient.

Mathematical modeling and dynamic simulation have become essential tools for designing and predicting the performance of reactors. However, the inherent difficulties of mimicking the complex porous bed structure in conventional simulations have typically resulted in models that do not include the fluid dynamic behavior present in biofilters and biotrickling filters (Lebrero et al., 2012; San-Valero et al., 2018). In this context, Computational Fluid Dynamics (CFD) simulations may become a helpful modeling tool that allows the reactor three-dimensional (3D) representation. CFD uses numerical methods to analyze fluids moving throughout packed bed columns. Recently, CFD coupled with computational tomography (CT) has been applied to study preferential flows in a packed bed biofilter (Moreno-Casas et al., 2020a) and to describe the gas-liquid mass transfer coefficient in a biotrickling filter (Moreno-Casas et al., 2020b), showing the potential of these techniques in the understanding of the processes undergoing on gas-phase bioreactors. CT has also been used to obtain images of the biofilm inside the porous media using contrast agents (Carrel et al., 2017, 2018), which seems a promising tool for studying the flow patterns over the local biofilm formation in biofiltration systems. For CFD-CT studies, validation against experimental data becomes crucial when generating a reliable, reproducible, and scalable model (Wicklein et al., 2016). For instance, CFD-CT models have been validated against experimental data based on pressure drops (Moreno-Casas et al., 2020a) and gas-liquid mass transfer coefficients (Moreno-Casas et al., 2020b). However, none of the above works has validated the modeled gas flow distributions inside the reactor, which is relevant for understanding and improving its design.

Procedures for validating the flow pattern of CFD models are commonly based on experimental RTD data measured in the liquid phase. Hydrodynamic characterizations in biofilters based on the liquid phase have been performed in previous research (Gunjal et al., 2003; Prades et al., 2017; Sharvelle et al., 2008; Trejo-Aguilar et al., 2005). However, the experimental liquid phase RTD does not validate the gas phase preferential flows and maldistribution, which limits their application in validating multiphase models that consider a gas/liquid interface. Thus, gas phase RTD is also required for a complete fluid dynamic characterization. In this way, Metal oxide (MOx) sensors can be used in RTD measurements and accurately quantify single gases and mixtures. Moreover, they are low-cost, can be easily

integrated into electronic circuits (Schmuker et al., 2016), and have been successfully used for environmental monitoring as a static (Martinez et al., 2019b; Schmuker et al., 2016) and mobile electronic nose (Monroy et al., 2012). Hence, implementing this low-cost technology may become useful to validate the gas flow RTD inside biotrickling filters.

In summary, the use of CFD-CT modeling validated with RTD techniques for liquid and gaseous flows can be applied to study the influence of the flow behavior in biotrickling filters, that in addition to the use of CT and biomass tracers may help understand the correlation between the physical processes undergoing during operation and the biofilm formation.

1.1 Hypothesis

Based on the previous information, the hypothesis addressed in this study is:
"It is possible to analyze the influence of the fluid dynamic behavior over the local biofilm formation inside the realistic description of the porous media in biotrickling filtration of VOCs by coupling 3D CFD-CT models with biofilm imaging techniques."

1.2 Objectives

General Objective

To develop a novel methodology to broaden the understanding of the influence of the fluid dynamic behavior inside biotrickling filters using CFD-CT techniques validated experimentally by RTD tests, to obtain the mass transfer coefficient, and biofilm formation through computational imaging techniques.

Specifics Objectives

i) To apply a low-cost metal oxide sensor capable of reproducing a gas tracer's concentration in real-time.

ii) To perform a fluid dynamic experimental characterization of a biotrickling filter in terms of RTD of the gas and liquid phases, as well as the volumetric global mass transfer coefficient determination.

iii) To validate a 3D CFD-CT simulation of the fluid flows inside the biotrickling filter with experimental results regarding the RTD and the volumetric mass transfer coefficient estimation.

iv) To analyze the feasibility of assessing the spatial distribution of the local biofilm formation over the packing material surface using computational tomography with contrast.

1.3 Organization of this document

Chapter 2 presents a literature review summarizing this thesis's most crucial information, including the current techniques for understanding the mechanisms governing biotrickling filters. Chapter 3 presents the materials, experiments, and simulation methods to attain the proposed objectives. Chapter 4 summarizes the results obtained, comparing them with relevant information from the literature. Finally, Chapter 5 outlines the conclusions of this thesis and states future research directions and opportunities.

2 LITERATURE REVIEW

2.1 MECHANISM AND PARAMETERS OF BIOTRICKLING FILTERS

BTF systems consist of a tubular packed bed reactor inoculated with microorganisms from an external source, where polluted air is carried through the packing to be degraded. This reactor configuration is continuously or periodically irrigated with an aqueous solution (mineral salt medium) which contains the essential salts and minerals required by the microorganisms attached to the surface of the packing material to form a biofilm (Figure 1). Biofilms are communities of microorganisms attaching and developing on surfaces embedded in a matrix of extracellular polymeric substances (EPS) (Carrel et al., 2018), forming porous structures (up to 90 % porosity) with high water content (Wagner et al., 2010). To achieve the degradation of the pollutants, they must be transferred from the gas phase into the liquid phase and, later, from the liquid phase into the biofilm, where the compound is degraded by the microorganism and transformed into a source of energy or carbon.

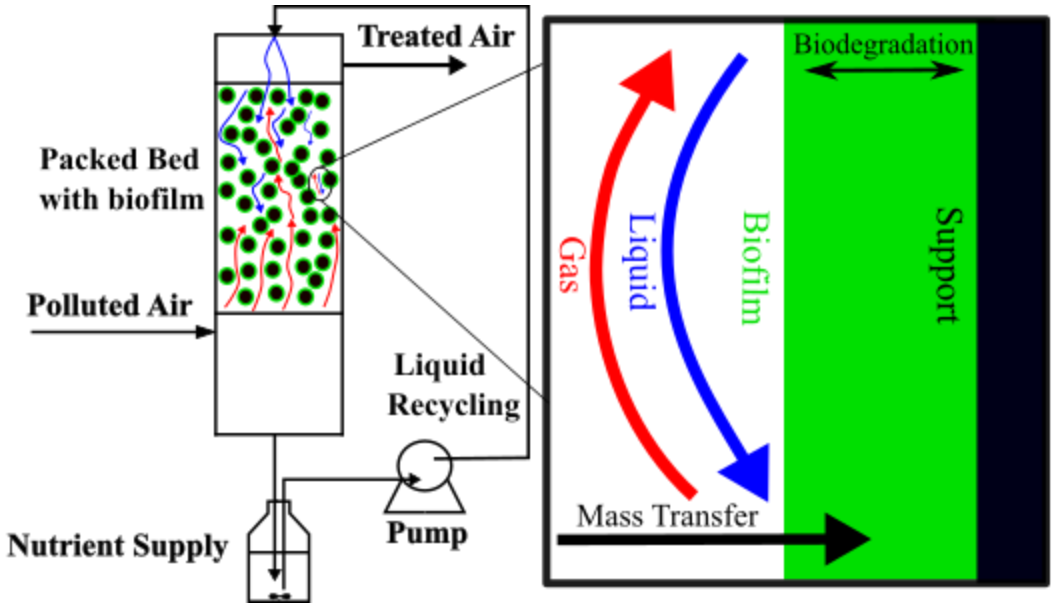

Figure 1. **Biotrickling filter mechanism.**

The first step involves transferring the pollutants and the oxygen from the gas to the liquid phase. This transfer happens in the interface between the phases, and the effect of the resistance in the gas phase can be neglected due to the similar transport properties of the air streams and the pollutants (Alonso et al., 1998a; Baltzis et al., 2001). Thus, it can be assumed that concentration in the gas-liquid is in equilibrium and can be represented by Henry's Law. In fact, due to the presence of the liquid phase, these reactors are adequate for treating compounds with a moderate-high solubility in water, with Henry constants lower than 0.1 (Kennes & Thalasso, 1998).

Later, the pollutants absorbed in the liquid phase are transferred into the biofilm. The mass transfer resistance between these phases occurs mainly when the pollutant is highly soluble in the liquid phase (Kim & Deshusses, 2003). However, due to the moderate solubility of VOCs in the liquid phase, this transfer is mainly caused by molecular diffusion. The gradient flux can be obtained from Fick's First Law, as the resistance to the mass transfer between the liquid-biofilm phase is negligible (Baltzis et al., 2001; Baquerizo et al., 2005; Sharvelle et al., 2008). The biodegradation occurs primarily inside the biofilm, where additional metabolites can also be produced. Due to these complex phase interactions, biotrickling filters can operate under mass transfer and/or biodegradation limitations (Kraakman et al., 2011).

2.1.1 Temperature

Temperature is one of the main parameters involved in biological processes that could affect mass transfer and biodegradation limitations. While the rise of temperature results in higher Henry's constants (less solubility of oxygen and pollutants into the liquid phase), it improves diffusion inside the liquid phase, enhancing the diffusion into the biofilm. However, this effect might be insignificant in operational conditions where the range of temperatures oscillates between 18-30°C (Diks & Ottengraf, 1991; Hartmans & Tramper, 1991).

2.1.2 pH

A neutral pH between 6.5-7.5 is the optimal range for heterotrophic microorganisms degrading VOCs (Lith et al., 1997). Nonetheless, intermediate metabolite accumulation in long-term operation may translate into lower performances due to their effect on the pH variation (Devinny & Hodge, 1995).

2.1.3 Nutrient solution.

A rich nutrient solution is fundamental in maintaining the biofilm (Lee et al., 2010) and must be renewed periodically. In addition, the proper renewal rate of this solution can regulate the pH instead of directly adding acid/base solutions to the external agitation tank.

2.1.4 Dissolved oxygen

This parameter is fundamental for achieving enough oxygen availability in the biofilm. Oxygen constraint is the limiting step for treating hydrophilic VOCs (Kirchner & Wagner, 1992). In contrast, for hydrophobic compounds, such as toluene or hexane (high Henry constant), the VOC mass transfer between the gas-liquid phase becomes the limiting step (X. Zhu et al., 2004).

2.1.5 Pressure drop

This parameter is an effective operational measurement to estimate the excessive

accumulation of biomass inside the packed bed that could result in lower system performance (Kennes et al., 2009). This accumulation reduces the pollutant residence time inside the column and enhances the formation of dead zones and preferential paths. In addition, high-pressure drops result in higher costs for energy sources.

2.1.6 Microbial community.

The start-up of BTFs requires an external source of microorganisms as the initial inoculum. The selection of these inoculums depends on the pollutant's biodegradability and packing material characteristics. The inoculum can be a pure culture, mixed culture, or adapted culture. The proper selection may improve the start-up of the process (Cox & Deshusses, 2001).

2.1.7 Liquid recirculation.

This operational parameter is fundamental to maintaining the system's humidity, nutrient concentration, and pH. The superficial trickling liquid velocity (TLV) affects the performance of the reactor when exceeding a critical value that provokes detachment of the biofilm in the packing surface. Generally, the standard values are below 10 m h^{-1} (Kim & Deshusses, 2008a). High velocities result in more wetted surfaces over the packing bed (Diks & Ottengraf, 1991), which improves the formation of local biofilm and may improve the gas-liquid mass transfer (Hartmans & Tramper, 1991), which translates into more oxygen and pollutant concentrations available in the biofilm. Nevertheless, as the operation at higher velocities results in biofilm detachment and the packing distribution may affect the mass transfer interface between the gas and liquid phases, its influence on the performance is still misunderstood. Recently, two-phase partitioning bioreactors have been widely used to treat hydrophobic VOCs as hexane or methane, as the addition of an organic phase in the recirculating liquid boosts the gas-liquid mass transfer (Pascual et al., 2021).

2.1.8 Gas flow.

The influence of the gas flow rate and inlet concentration on the biotrickling performance relies upon their influence over the performance parameters commonly used in biofiltration

systems, which are the empty bed residence time (EBRT, s), elimination capacity (EC, g m^{-3} h^{-1}), inlet load (g m^{-3} h^{-1}) and removal efficiency (%) that are calculated using the following equations:

$$EBRT = \frac{V_{bed}}{Q_G} \quad (1)$$

$$EC = \frac{Q_G}{V_{bed}}(C_{G,in} - C_{G,out}) \quad (2)$$

$$IL = \frac{Q_G}{V_R}(C_{G,in}) \quad (3)$$

$$RE = \left(\frac{C_{G,in} - C_{G,out}}{C_{G,in}}\right) \cdot 100 \quad (4)$$

Where Q_G is the gas flow rate (m^3 h^{-1}), V_{bed} is the packing bed volume of the BTF (m^3), and $C_{G,in}$ and $C_{G,out}$ are the inlet and outlet concentrations of the gas pollutant (g m^{-3}), respectively. The EBRT is the relative measure of how long gas is retained within the packing material and critically affects the treatment performance of BTFs (Rene et al., 2010; Wu et al., 2018a). This parameter has a range of values that go from tenths to hundreds of seconds, higher in the initial stages of operation and decreasing as the steady state is reached (Runye et al., 2015). The elimination capacity vs. inlet load curve is typically obtained during the biotrickling operation to estimate the maximum elimination capacity. The assumption is that the performance depends only on the pollutant load. However, this assumption is invalid for concentrations lower than 0.1 g m^{-3} for pollutants with high Henry's constant values due to the mass transfer limitations (Kennes & Veiga, 2001). Thus, operations under low concentrations with high flow rates will not lead to elimination capacities obtained for high concentrations with low flow rates. Nonetheless, the use of this curve after the biotrickling filter is on a steady state (constant elimination capacity under a specific constant gas inlet flow rate and TLV) allows for studying the influence of increasing the inlet load over time (Vergara-Fernandez et al., 2020). This experience converges to a maximum elimination capacity which represents the intersection between the operational condition where the system is under mass transfer limitation ($EC < EC_{max}$) or under biodegradation kinetics

limitation ($EC = EC_{max}$) for a constant EBRT and TLV.

2.1.9 Packing material

It is one of the core parameters involved in the design of BTFs. The packing material must satisfy crucial requirements such as low cost, low weight, chemically stable, high surface area, high porosity, and optimal environmental conditions to sustain the attachment and growth of microorganisms (Cox & Deshusses, 2001; Wu et al., 2018b). Different factors such as specific surface area, moisture retention, density, resistance to compaction, adsorption properties, and nutrient supply determine the proper packing material's characteristics (Dorado et al., 2010). In BTFs, the packing material is usually inert (requires an external source of microorganisms) with high porosity and specific surface areas in the range of 100-400 $m^2 m^{-3}$ (Revah & Morgan-Sagastume, 2005). Yang et al. (2011) and Caicedo et al. (2018) studied the impact of using polyurethane foam as structured packing or as random packing in the biotrickling filtration of toluene. However, their conclusions were different regarding which packing configuration improved the performance. The difference is that in Caicedo et al. (2018), the study was carried out with different liquid phase recirculation rates, resulting in different wetted areas for a specific configuration.

Additionally, these studies did not consider the influence on the gas and liquid flow distribution performance and the presence of channeling and dead zones. Given the above, the long-term goal of this thesis is to improve the understanding of the fluid dynamic behavior resulting from the interaction of the packing material with the gas and liquid flows over the mass transfer and the local biofilm formation. Thus, the main parameters studied in this thesis are the effects of the packing material configuration, the gas flow, and the liquid flow over the limitation mechanisms.

2.2 BIODEGRADATION KINETICS ESTIMATION

In BTFs, the research has mainly focused on biodegradation kinetics rather than mass transfer characterization (Dorado et al., 2009). The former studies are mainly based on determining the biokinetic parameters adapted from suspended biomass, which implies biofilm destruction (Yurt et al., 2003). Thus, these values are inconsistent with the mass transfer over

the biofilm surface (Bonilla-Blancas et al., 2015; Hille et al., 2009; Mannucci et al., 2012). Furthermore, this approach does not consider the physiologic differences between suspended and attached biomass, resulting in the overestimation of microbial activity in gas treatment systems. Research about biokinetics in biofilms is still under study because most previous results have been carried out considering only the internal mass transfer when the biofilm is also dependent on the external mass transfer (Ordaz et al., 2019). Heterogeneous respirometry techniques have been successfully applied to estimate transport and biological phenomena (Bonilla-Blancas et al., 2015). However, they depend on data based on the substrate degradation inside the biofilm, which is challenging to obtain.

In this thesis, the biodegradation kinetics are not considered in the model, and only the local biofilm formation due to the flow behavior will be studied.

2.3 MASS TRANSFER COEFFICIENT ESTIMATION

Mass transfer in biotrickling filters involves transporting the target pollutant and oxygen from the gas phase into the liquid phase through the gas-liquid interface and, later, an additional transport from the liquid phase into the biofilm through the liquid-biofilm interface. This transport depends on the physical properties of the gaseous contaminant, the liquid phase, the packing material properties, and the operational conditions. Because process limitations result from the different interactions between the operational variables and the design of the biofilter, mathematical models have been developed to seek improvement of knowledge about the treatment process. The aim focuses on understanding the effect of the variation of these operational parameters and thus predicting the global performance of the system, saving excessive consumption of time and resources (San-Valero et al., 2018). In BTF, the plug flow model is used to reproduce the movement of the liquid and gas inside the reactor. Occasionally, the axial dispersion must be evaluated for its influence on the performance of the process. Some authors have indicated that this effect was insignificant, except in biofilters that work at residence times of a few seconds (Devinny & Hodge, 1995). The latter assumption was made considering conventional biofilters, while in BTFs, the residence times are shorter, which may be significant when analyzing mass transfer inside the column. The external mass transfer is often estimated by modeling the mass transfer coefficients relating the gas phase to the liquid phase using Henry's constant, which relates the contaminant

concentration at the interface according to the two-film theory. This theory allows for calculating the concentration of contaminant transferred to the liquid phase under the operating conditions of the reactor (Cristian et al., 2000; Kibazohi et al., 2004; Kim & Deshusses, 2008b). The transfer velocities are defined as the mass transfer rate coefficients and are used to obtain the resistance to the mass transfer according to the following equation:

$$\frac{1}{k_{overall}} = \frac{1}{k_G} + \frac{1}{k_L} + \frac{1}{k_B} \tag{5}$$

Where k_G is the mass transfer coefficient for the gas phase, k_L is the mass transfer coefficient for the liquid phase, k_B is the mass transfer coefficient for the biofilm, and $k_{overall}$ is the combination of the different mass transfer coefficients involved in the process. Usually, the mass transfer in the gas and biofilm is neglected due to the low concentration of pollutants, and the transfer rate can be described by the following equation proposed by Koch (1990):

$$k_L a \left(\frac{C_G}{H} - C_L\right) = \left(\frac{\mathcal{D}_{GL}}{\delta_L}\right) a \left(\frac{C_G}{H} - C_L\right) \tag{6}$$

Where $\mathcal{D}_{GL}$ is the target gas pollutant diffusivity in the liquid phase, H is the Herny coefficient, δ_L is the liquid film thickness, and C_G and C_L are the pollutants concentrations in the gas and liquid phases, respectively. The term k_L is the mass transfer coefficient, a is the specific interfacial area between the gas-liquid interface and the term $k_L a$ is the volumetric mass transfer coefficient consisting of all independent factors that determine the mass transfer rate (Kraakman et al., 2011). This theory's advantage is that it leads to simple expressions to estimate the gas-liquid mass transfer, which is helpful for basic practical applications. However, the two-film, penetration, and surface renewal theories do not account for local variations of the fluid velocities, physical properties, or flow regimes (Wang et al., 2018). Table 1 shows studies that obtained the mass transfer coefficient in biotrickling filters for toluene and oxygen, which are the gas targets in this thesis. These studies share a similar methodology and experimental procedure by obtaining the concentrations in the outlets employing gas chromatography and then using correlations (Dorado et al., 2009). However, the transfer coefficients are often estimated using correlations obtained from packing materials used in gas absorption, desorption, or distillation, which have been estimated under different flow regimes from those used in biofiltration leading to the overestimation of these

values (Kim & Deshusses, 2008b). In Wang et al. (2005), the different correlations used in packed columns were analyzed, concluding that they lack knowledge about the transport phenomena that occur inside the porous zone, emphasizing the need for research that considers detailed dynamics of the involved flows. In addition, Parnian et al. (2017) observed discrepancies when adjusting experimental data with these models due to not considering fluid dynamic aspects, such as stagnant zones, dead volumes, and channeling effects.

Table 1. Comparison of $k_L a$ values reported for toluene and oxygen in BTFs

Target gas	**Packing Material**	**EBRT [s]**	**TLV [m h^{-1}]**	**$k_L a$ [h^{-1}]**	**Reference**
Toluene	Polyurethane Foam	11-50	0.6	35-90	(Lebrero et al., 2012)
	Clay pellets	6-100	2	12-258	(Dorado et al., 2009)
	Lava rocks			10-150	
	Dixon rings			10-199	
				11-415	
	Steel Pall rings	32-144	3.3-4.7	10-60	(Pedersen & Arvin, 1995)
	Polypropylene rings	2.4	15.3-50.8	0.9-1.2	(Heymes et al., 2006)
Oxygen	Polypropylene rings	104-312 m h^{-1}	3-30	20-100	(San-Valero et al., 2012)
	Polypropylene rings		2-33		(San-Valero et al., 2014)
	Structured Media			20-200	
	Polypropylene rings	15-30	10	46.8	(San-Valero et al., 2018)
	Polyurethane Foam	12-240	0.6-5	30-300	(Estrada et al., 2014)

Additionally, the use of the EBRT as a design parameter differs from the real residence time of the gas inside the packing, resulting in overestimated parameters such as the effective volume of the bed, the porosity, and the velocity of the flows. In Kim & Deshusses (2008b), a method to characterize the mass transfer for different packing materials used in biotrickling filtration was proposed to develop new correlations. However, the characterization required large concentrations of NaOH in the recirculating liquid phase (40 g L^{-1}), which is much higher than the concentration of salt used as nutrients. Additionally, these techniques do not provide insight into the gas and liquid flow behavior inside the packed column (Moreno-

Casas et al., 2020b). Lebrero et al. (2012) concluded that the characterization of mass transfer is a powerful tool to optimize the design and operation of BTFs. However, the lack of general and straightforward models limits the optimal design of these reactors based on mass transfer parameters. In addition, researchers have been emphatic about the need to develop simulations for the design and optimization of BTFs that allow the effective estimation of the mass transfer coefficient to facilitate the selection of the packing material and the modeling of bioreactors (San-Valero et al., 2014). Thus, a theory that describes the fluid dynamic characterization is required.

In contrast to the theories above, the boundary layer theory considers the fluid dynamic effect (Dutta, 2009), providing a detailed interpretation of the local mass transfer in more realistic models like the one implemented in this thesis. The boundary layer theory considers that the concentration distribution of the pollutant within the air boundary layer is a function of its location, $C_{A,G}(x,y)$, its thickness, δ_G, and the distance from the plate leading edge (Dutta, 2009). Thus, the momentum diffusivity and the mass diffusivity play a key role in the overall mass transfer phenomena, which can be accounted for with the Schmidt number, Sc (Moreno-Casas et al., 2020).

If the momentum diffusivity is larger than the mass diffusivity, Sc is larger than 1 and ${}^{\delta}/_{\delta_G} = Sc^{1/3}$ (Bird et al., 1960) . The average plate Reynolds number, Re_l, and the average Schimidt number, Sc_{av}, can be used to define the average Sherwood number as follows:

$$Sh_{av} = \frac{K_L l}{\mathcal{D}_{AB}} = 0.664(Re_l)^{1/2}(Sc)^{1/3} \tag{7}$$

$$Re_l = {\rho u_\infty l}/{\mu} \tag{8}$$

$$Sc = \frac{\nu}{\mathcal{D}_{AB}} \tag{9}$$

Where K_L is the average mass transfer coefficient along the plate length, u_∞ is the gas free stream velocity, right above the end of the boundary layer, ρ the fluid density, ν the kinematic viscosity of the fluid, μ the dynamic viscosity of the fluid and $\mathcal{D}_{AB}$ is the diffusion coefficient between fluids A and B.

Rearranging the expression, the computation of the mass transfer coefficient can be obtained

by applying the following equation:

$$K_L = 0.664(l)^{-1/2}(u_\infty)^{1/2}(\nu)^{-1/6}(\mathcal{D}_{AB})^{2/3} \quad (10)$$

2.4 COMPUTATIONAL FLUID DYNAMICS (CFD)

Computational Fluid Dynamics (CFD) is a powerful modeling tool that allows the three-dimensional (3D) representation of reactors and uses modeling and numerical methods to solve and analyze fluid dynamics problems. CFD offers the possibility of describing even complex fluid dynamics for single or multiphase systems and transport processes under different operational conditions. This modeling tool computes the pressure and velocity field based on the non-linear, partial differential equations known as the Navier-Stokes equations (Hinkelmann, 2005). In the context of biofiltration systems, CFD models can help estimate fluid patterns' performance and influence on pollutant transport and mass transfer. In order to determine the flow field and transport in complex porous zones, time and space are discretized through different numerical methods, leading to an approximated solution, which must be reasonably close to reality (Ferziger & Perić, 2002). These approaches can be a one-dimensional (1D), two-dimensional (2D), or three-dimensional (3D) approach. The 1D approach models are commonly used when the effects in two of the three dimensions can be neglected. In contrast, the 3D model is preferred to capture detailed information about the flow's combined effects with the reactor environment. Thus, instead of simplified 1D simulations, the local small-scale effects, such as local mass transfer coefficients and biofilm formation can be analysed using the three-dimensional approach.

For the three-dimensional model description of reactors, the open-source CFD software OpenFOAM offers the possibility to solve complex partial differential equations by choosing one of the multiple solvers and utilities available for different numerical problems. OpenFOAM contains pre-processing and post-processing environments that can describe 2D and 3D simulations (Greenshields, 2022). The partial differential equations are discretized based on the Finite Volume Method in space and the Finite Differences method in time (Manafpour & Ebrahimnezhadian, 2017). A model setup in OpenFOAM can be divided into three steps: pre-processing, solving, and post-processing.

The pre-processing step generates the computational mesh and defines the boundary and

initial conditions. A computational mesh is needed in order to solve the relevant equations. The computational domain is divided by generating the mesh into a finite number of volumes where the solution is calculated. The number of selected cell volumes (space discretization) influences the calculation effort and the accuracy of the results. Structured meshes can be created with different mesh generators such as *blockMesh*, *snappyHexMesh* (Greenshields, 2022), and *cfMesh* (Juretic, 2017), each with different advantages and disadvantages. Developing a high-quality 3D mesh is a complex and time-consuming process, but the effect of the mesh quality on the simulation results is significant and should not be underestimated.

Later, the boundary and initial conditions must be defined for each variable being solved. Good initial conditions can lead to faster convergence. For boundary conditions, the user can define Dirichlet (fixed concentration), Neumann (fixed dispersive flux), and Cauchy (fixed total mass flux) or a combination of them.

The governing equations for the single-phase flow of an incompressible Newtonian fluid under isothermal conditions with only gravity as body force are given by the continuity equation and the conservation of linear momentum equations (Nieves-Remacha et al., 2015).

For multiphase flow simulations, some different solvers are available in OpenFOAM. Multiphase flows can be classified in different ways, and depending on their classification, a different kind of solver can be chosen (Manafpour & Ebrahimnezhadian, 2017).

A phase is a defined material with homogeneous characteristics, which can also be different physical states of one fluid. Thus, multiphase flows can then be classified by the physical state of the different fluids as well as the topology of the interface between these phases. For example, gas phases can be compressible or incompressible depending on the flow velocity and temperature. The properties of the interface can be differentiated between separated or dispersed flows (where separated flows are not mixed) sharing a continuous interface, and both phases generally share the same velocity. On the other hand, dispersed flows may consist of continuous and dispersed phases. Thus, the interaction of these phases occurs through penetration, and the interface between phases is not continuous (Manafpour & Ebrahimnezhadian, 2017).

2.4.1 CFD-CT applications in biological systems

The main advantage of the 3D models applied in biofiltration systems is capturing the porous structure inside the packed bed. For example, Rahul et al. (2012) compared two models for benzene degradation in a biofilter using a standard convection-advection reactor model and a CFD model. They found that the CFD model predictions were more accurate, although the description of the packing material was not fully disclosed and did not seem to be based on a detailed description of the packing. Amani et al. (2018) simulated a packed-bed reactor for the biological treatment of phenol using a CFD 3D approach. However, the packing material was assumed to be completely uniform in size and completely spherical. Prades et al. (2017) simulated the liquid velocities and oxygen consumption on a flat plate bioreactor by coupling CFD with biological reactions showing good approximations and the potential for optimization of the performance of these reactors. Nevertheless, the latter work did not consider the packing bed structure. Soulaine et al. (2018) and Mirabolghasemi et al. (2015) coupled the CFD models with digitalized porous images to analyze flows in porous media, showing the feasibility of obtaining characteristic parameters of the structure as porosity and permeability.

Recently, CFD techniques coupled with computational tomography (CT) have been applied to perform CFD simulations under realistic packing bed descriptions, which is fundamental to improving the knowledge of the flow behavior inside these complex structures. For example, Moreno-Casas et al. (2020a) performed a CFD-CT simulation to estimate preferential flows and channeling inside the packing bed in a conventional biofilter. Additionally, Moreno-Casas et al. (2020b) studied the potential of CFD to describe the mass transfer between the gas and liquid phases in an abiotic biotrickling filter using oxygen as a reference gas. The computational domain was set as the actual polyurethane sponge structured support used in biotrickling filtration. This image was obtained by microtomography (μCT). The simulation was performed in 2D on an intermediate sector of the packing using the Volume of Fluid method to determine the gas-liquid interface. This study demonstrated the potential to estimate global volumetric mass transfer coefficients using the boundary layer theory, which, unlike the two-film theory, does consider the fluid dynamic effect.

In addition, X-ray tomography and magnetic resonance imaging (MRI) have been used to access biofilm morphology in porous media at the mesoscale. The mesoscale links the micro- and the macro scale, as it is the scale at which flow and mass transfer interact and define the biofilm structures (Eberl et al., 2000). This methodology should allow the study of biofilm visualization inside the porous structure in biotrickling filters, which, to the author´s knowledge, has not been done before.

For example, Caizán-Juanarena et al. (2019) used MRI to obtain images of biofilm inside activated carbon, showing that the high resolution of the MRI allowed for capturing the biofilm thickness. However, the application of MRI to the study of biofilm formation in porous media is limited due to the difficulties of accessing the device and the cost of the apparatus. Furthermore, contrast agents must be added to distinguish both phases due to the high-water content inside the biofilm, as their attenuation coefficients are similar. In addition, the selection of contrast agents depends on the packing material's X-ray absorption and must be easily differentiated from the biofilm (Davit et al., 2011). Medical suspensions of micrometer-size barium sulfate ($BaSO_4$) suspensions have been used as contrast agents to label non-biofilm colonized pores by enhancing the absorption of the water phase (Carrel et al., 2017, 2018; Davit et al., 2011) and potassium iodide (KI) to enhance the attenuation coefficient of the biofilm, to be distinguished from the packing material (Davit et al., 2011). In addition, these studies showed the potential of these techniques to assess the clogging and biofilm morphologies in 3D simulations. Nonetheless, neither of these studies analyzed the external mass transfer effect from a gas phase, which requires the validation of the flow simulation. Thus, it can be concluded that more experimental validation tools and model enhancements are necessary to obtain a more realistic description of the system.

2.4.2 Experimental validation of CFD models.

CFD models validated with experimental results are scarce. For example, Moreno-Casas et al. (2020a) validated the biofilter model by comparing the differential pressure obtained with a U-tube differential manometer with the resulting pressure gradient calculated with the momentum equation, which does not validate the flow profile inside the reactor. Moreno-Casas et al. (2020b) validated the biotrickling filter model by comparing the simulation values of the gas-liquid mass transfer coefficient (K_La) with experimental results obtained

with measurements of dissolved oxygen concentration in a stirred tank reactor using a DO probe connected to a C3020 multi-parameters analyzer (Consort, Belgium), which has 30 s delay time response at 25°C. However, previous validations of their velocity field are required to ensure the reproducibility of the mass transfer model at different gas-liquid flows. To properly validate the flow inside the reactor, the experimental velocity profile is required to ensure that the flow pattern is similar to the one given by the simulation. However, incorporating these sensors inside the reactor provokes a change in the natural flow pattern that results in validation errors compared with the simulation results if these sensors are not incorporated into the model. In this way, the RTD test is a well-known methodology employed to characterize the fluid dynamic behavior in diverse systems experimentally. Furthermore, this technique allows the analysis of the flow non-idealities inside the packing bed reactors and helps understand specific hydrodynamics effects such as channeling and flow maldistribution (Gunjal et al., 2003); thus, RTD is a well-suited experimental technique to validate the velocity profile of CFD simulations indirectly. Previous research has used this technique to assess hydrodynamic characterizations in biotrickling filters based on the liquid phase.

Sharvelle et al. (2008) used the step-change technique by injecting potassium bromide (KBr) as a tracer in the influent. They used a TDS (total dissolved solid) conductivity meter to monitor the KBr concentration over time. It was concluded that packing material selection plays a crucial role in the performance of biotrickling filters. In the same study, the requirement of future research on the effects of geometry and composition on the performance of BTFs was mentioned. Similarly, Trejo-Aguilar et al. (2005) used the pulse technique conducted by the injection of dextran blue as a tracer in the influent of a biotrickling filter to evaluate the effect of the porosity variations due to microbial growth over the performance. This study used a spectrophotometer at 650 nm to measure the absorbance of the tracer over time. It was concluded that a better understanding of the hydrodynamics might help improve the mass transfer coefficient estimation leading to a more rational design of these reactors. Finally, Prades et al. (2017) validated a flat plate bioreactor CFD model using the pulse technique by injecting methylene blue in the influent. They used a spectrophotometer to measure the concentration over time, suggesting that the application of these techniques in the modeling of bioreactors could develop more rigorous models that

may allow a better understanding of the role of hydrodynamics in the process. However, the liquid phase validation cannot be used to validate the gas phase preferential flows and maldistribution, which limits their application in the validation of multiphase models that consider a gas/liquid interface. A gas phase RTD is also required for complete multiphase hydrodynamic characterization. Research regarding the gas phase RTD has been conducted using O_2 and N_2 as a tracer in a fluidized bed (Lorences et al., 2006), using ozone in a steady flow of O_2 as the tracer in a falling-film microreactor (Commenge et al., 2006), helium as the tracer in a Fisher-Tropsch slurry bubble column (Han et al., 2019), as well as in a prismatic modular reactor (Said et al., 2018). Unfortunately, these tracers can be degraded by the biomass present in the biofiltration system while also requiring long response times. Mohamadi-Baghmolaei et al. (2019) used an AGILENT-7890A gas chromatographer with an automated gas sampling valve for online measurement of a gas phase to monitor gas compound concentrations (CO_2, N_2, and CH_4). However, this equipment is expensive to acquire and operate, making it unattractive for model validation.

Although appealing, RTD tests over the gas phase in biofilter reactors are scarce. For example, a pulse technique conducted by the injection of methane as a tracer used a Foxtobo TVA-1000 portable flame ionization detector (FID) detector to measure the concentration over time, concluded that the requirements for estimating the airflow that optimizes the substrate mass transfer for each packing bed are crucial in the design of these type of reactors (Prenafeta-Boldú et al., 2008). Similarly, a pulse technique conducted by injecting carbon dioxide (CO_2) as a tracer used a CO_2 analyzer (Horiba APBA-210 non-dispersive IR) to measure the concentration over time. It concluded that increased back mixing in the gas flow increased the maximum elimination capacity and the critical loading value (Hutomo and Pinder, 2006). Nevertheless, the principal drawback of this experience is the prohibitive cost associated with the lab schemes and sensors for gas concentration measurements. Also, using CO_2 as a tracer in biofilters with active biomass is not recommended due to the production of metabolic CO_2 when mixed with the injected CO_2, inducing erroneous measurements of the concentration. Therefore, developing a fast and low-cost RTD analysis methodology is crucial to validate CFD simulations for multiphase flow reactors.

2.5 METAL OXIDE SENSOR

Metal oxide (MOx) sensors can accurately quantify single gases and mixtures, are low-cost, and can be easily integrated into electronic circuits (Schmuker et al., 2016). The operational principle of this type of sensor is based on the capability of the metal oxide surface to absorb the molecules of oxygen present in the air, trapping the electrons that flow through the band in the form of ions. Therefore, the contact between the surface and a reducing gas results in a reaction of the oxygen molecules, allowing the electrons to flow, thus reducing the resistance as a function of the reduced gas concentration (Wang et al., 2010). These sensors have been used for environmental monitoring as a static (Martinez et al., 2019b; Schmuker et al., 2016) and mobile electronic noses (Monroy et al., 2012). However, their optimal detection range and the long recovery time (required between samples) can result in a major drawback when performing RTD analysis. In order to improve the signal behavior, different processing methods have been successfully applied based on the sensor time constants (Martinez et al., 2019a; Monroy et al., 2012; Schmuker et al., 2016). Nonetheless, their implementation to perform gas-phase RTD characterization in biofiltration systems has not been studied.

3 MATERIALS AND METHODS

3.1 COLUMN AND PACKING PROPERTIES

3.1.1 Packing material characteristics

Polybutylene rings were used as random packing material. Each ring had an approximate height of 15 mm with external and internal diameters of 19 and 17 mm, respectively. This material was selected because it is a low-cost, durable, non-biodegradable, well-known packing used in biofiltration and has physical properties compatible with computerized tomography. Additionally, the optical density threshold differs with the water and biofilm, allowing easier image reconstructions. The rings were glued using a PVC adhesive based on cyclohexanone to fix the whole structure and ensure that the geometrical distribution of the porous domain remained constant between the RTD experiments and the computational tomography scan. The adhesive application was completed weeks before the experiments to ensure that the entire structure was correctly fixed. The resulting porous structure had a height

of 0.40 m and a diameter of ≈ 0.115 m (Figure 2).

Figure 2. **Packed bed structure.**

3.1.2 Tubular reactor

The experiments were performed in a methacrylate tubular reactor with a working volume of 6.518 L, which consisted of a cylinder with a height of 0.566 m and an internal diameter of 0.115 m coupled at the bottom with a conical funnel with a height of 0.08 m (Figure 3). The gas inlet and outlet (8 mm inner diameter) were placed at opposite sides of the column at the height of 0.15 m and 0.58 m, respectively. The liquid inlet and outlet (15 mm inner diameter) were placed at the column's top and bottom. The packing material was placed 0.01 m above the gas inlet. The packed bed porosity was measured by water volume differences with an approximated value of 0.90.

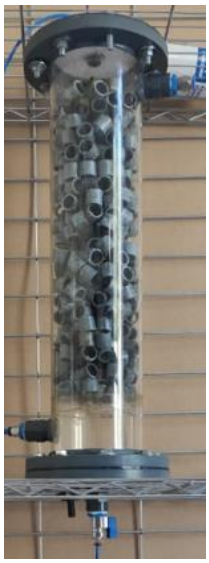

Figure 3. **Packed bed column.**

3.2 METAL-OXIDE SENSOR IMPLEMENTATION

3.2.1 Sensor characteristics

A FIGARO TGS813 series sensor, acquired from RS Components (Madrid, Spain), was used to carry out the gas tracer experiments (See Appendix A2 for the circuit diagram). This sensor is mainly composed of tin dioxide as the sensing element, has an optimal detection range between 500~10000 ppm of gas concentration in air, and has a high sensitivity to various reducing gases. This sensor has been selected due to its low cost and easy implementation. This device was mounted in an Arduino Uno Board coupled with a 16-bit analog-to-digital converter (ADC) connected to a standard USB port in a generic laptop/desktop computer for control and data acquisition, with an open-source software developed in Python 3.7 (Grinias et al., 2016). The circuit of the FIGARO TGS813 series sensor consists of a simple voltage divider and the variation of the resistance (R_s) can be obtained using Eq. (11):

$$R_s = \left(\frac{V_{cc}}{V_{RL}} - 1\right) \cdot R_L \tag{11}$$

Where R_L is the load resistance, V_{cc} is the circuit voltage applied across the sensor element and V_{RL} is the sensor signal measured indirectly as the change in voltage across R_L. The corresponding values of V_{cc} and R_L used in this work were $5\ V$ and $10\ k\Omega$, respectively.

3.2.2 Gas tracer

Butane acquired from Butsir (Barcelona, Spain) was selected as the gas tracer in this study due to its well-known characteristics, easy handling, and high sensitivity with the sensor.

3.2.3 Signal reconstruction model

The mathematical model proposed by Monroy et al. (2012) was herein used to filter the sensor's slow recovery time due to its easy implementation and validation under similar conditions. Thus, the signal under a steady state was obtained from the raw data measured by the sensor. This model divides the sensor into three stages: The measurement circuit stage, the transient behavior stage, and the transduction stage.

Initially, the transient resistance is obtained from Eq. (11) in the measurement circuit stage. Subsequently, the steady-state resistance is recovered in the transient behavior stage using Eq. (12):

$$R_1(t) \propto R_2(t) + \tau_i \frac{R_2(t) - R_2(t\ -\ 1)}{\Delta t} \tag{12}$$

Where Δt is the data acquisition rate, τ_i could be the time constant of the rising phase τ_r or the recovery phase τ_d, and $R_1(t)$ and $R_2(t)$ are the resistance under steady-state and under transient behavior at time step t, respectively. Both time constants were obtained immediately before the RTD experiments to ensure that these values were calibrated under the same environmental and operational conditions. This calculation was achieved by evaluating the signal behavior upon different step responses under the operational conditions of the RTD experience (Ogata, 2010). A bi-exponential time-dependent response, $r(t)$, was used to calculate the response times constants when the step stimulus reached 63.2% (Figure 4, panel A) of its total change (Schmuker et al., 2016) using Eq. (13):

$$r(t) = -\frac{\tau_r}{\tau_r - \tau_d}\left(e^{-\frac{t}{\tau_d}} - e^{-\frac{t}{\tau_r}}\right), \quad for\ t \geq 0 \tag{13}$$

These parameters were obtained by injecting different concentrations of butane over the sensor surface as a step stimulus with a 10 mL gas-tight Hamilton syringe while the sensor

was exposed to a constant airflow of 8 L min^{-1} measured with a variable-area rotameter V series (Aalborg, USA). The flow effect was assessed to introduce its behavior over the calibration (Figure 4, panel B). The sensor was set at a data acquisition rate of 20 Hz and graph periods of 20 s per stimulus. The data obtained were post-processed using the libraries NumPy and Pandas from Python 3.7. Firstly, the maximum signal value was extracted to find the separation point between the rise and the recovery phase. Secondly, a linear interpolation of 63.2% of the peak voltage value was applied for each step stimulus to determine the time constant for the rise phase over the gas flow. Finally, the same methodology was used to obtain the recovery time constant.

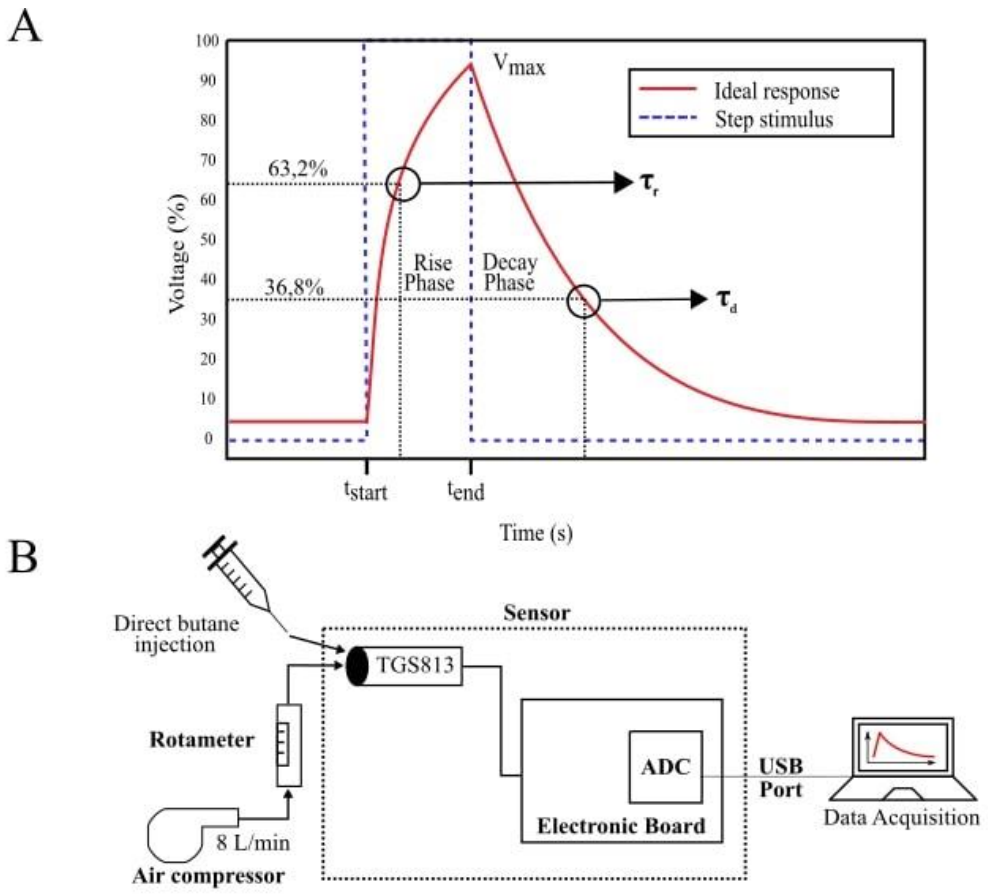

Figure 4. **MOx sensor response time constant determination**. (A) Ideal sensor response over a step stimulus under a steady state. The rise phase is the time range between the first stimulus and the maximum signal measurement. The decay phase corresponds to the time

between the maximum measurement and the total time recovery of the signal**.** (B) Schematic representation of the experimental setup used to determine the sensor response time constants

In the transduction stage, this data was post-processed to a normalized resistance value (R_s/R_0) to estimate the tracer concentration using the technical information provided by the manufacturer (Appendix I). The value R_0 corresponds to the sensor resistance at 1000 ppm of methane under atmospheric conditions. In this study, the influence of humidity and temperature on R_0 was neglected since the experiments were carried out under similar operational conditions to those used in the sensitivity curve. This value was obtained by measuring the sensor resistance inside a plastic container adapted to let the sensor hang in the middle of the container and injecting 70 µL of pure methane with a 500 µL gas-tight Hamilton syringe to obtain concentrations near 1000 ppm inside the container. Finally, the resistance R_0 was calculated with Eq. (11) and used to obtain the concentration values of the tracer using the manufacturer sensitivity data (Appendix A1).

3.3 RESIDENCE TIME DISTRIBUTIONS

3.3.1 Gas phase RTD

The flow behavior of the gas phase was assessed using the RTD test. Butane-laden airflow moving through the packed bed reactor was controlled with a rotameter at 8 L min^{-1}, which entailed an EBRT of 48.885 s. The gas tracer injection port consisted of a glass tube Afora™ V83120 (Afora S.A, Spain) capped with a butyl septum installed in the gas inlet pipeline 0.06 m before the column inlet (Figure 5). The MOx sensor was programmed to monitor the voltage over time with a data acquisition rate of 20 Hz and a graph period of 200 s per injection. A 10 mL butane pulse was injected manually using a 20 mL conventional polypropylene syringe. Before each experiment, clean air was pumped into the column to remove the volatile residuals produced from the glue that could distort the sensor signal. These experiments were carried out in triplicate.

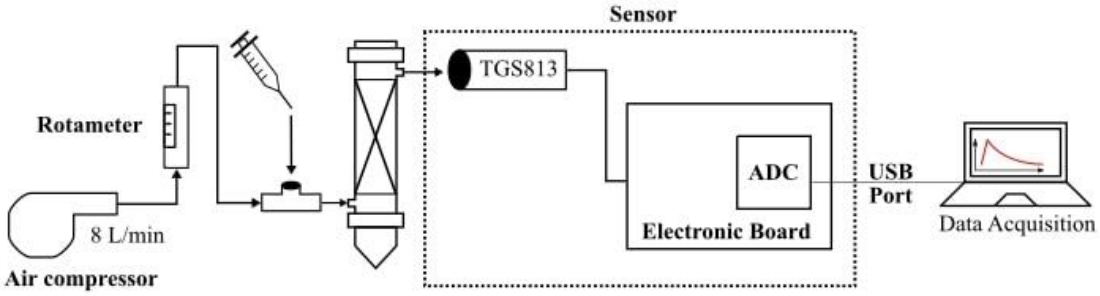

Figure 5. **Schematic representation of the experimental setup used to determine the gas residence time distribution**.

3.3.2 Liquid phase RTD

A water flow moving through the packed was circulated from an external water tank using a peristaltic 520-S pump (Watson Marlow, UK) with a trickling velocity of 2 m h^{-1}, which entailed a liquid flow of approximately 0.4 L min^{-1}. The fluid tracer injection port consisted of a glass tube Afora™ V83120 (Afora S.A, Spain) capped with a butyl septum installed in the liquid inlet pipeline 0.01 m before the liquid inlet at the top of the column (Figure 6). A 10 mL pulse of 0.1 g L^{-1} methylene blue solution was injected manually using a 10 mL conventional polypropylene syringe. Immediately after the infection, 1 mL samples were recovered at the bottom of the column in 1 mL Eppendorf tubes for 30 seconds in lapses of about one second of difference. Due to the difficulties of establishing a constant data acquisition rate of the samples, the whole procedure was recorded by video, and the sampling times were obtained from the video analysis. Finally, the optical density of the samples was measured by spectrophotometry at 668 nm (UV-2550, Shimadzu, Japan). Before each experiment, the column was cleaned with distilled water until the absorbance of the water samples at the outlet of the column was equal to zero. These experiments were carried out in triplicate.

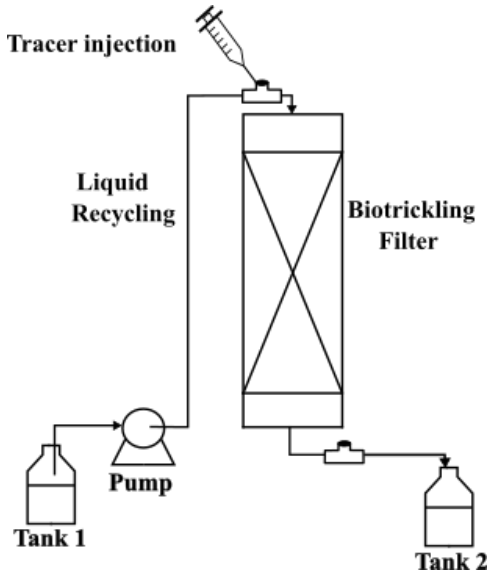

Figure 6. **Schematic representation of the experimental setup used to determine the gas residence time distribution.**

3.3.3 RTD mathematical model

The RTD function $E(t)$ is a probability distribution function that describes the time that a fluid element stays in the reactor and is defined by Eq. (14):

$$E(t) = \frac{C(t)}{\int_0^\infty C(t)\, dt} \tag{14}$$

Where $C(t)$ is the monitored concentration of the tracer at the reactor outlet over a time t.

This function can be used to understand the flow behavior and the mixing patterns inside the reactor, becoming an essential tool for estimating the non-idealities inside reactors (Singh et al., 2018). The proper analysis of this function is accomplished by quantifying the RTD function's moments to analyze the reactor's performance.

The mean residence time t_m describes the first moment and can be obtained by applying Eq. (15):

$$t_m = \int_0^\infty tE(t)\, dt \tag{15}$$

In packed bed reactors, this parameter is used to analyze the presence of dead zones and bypasses by comparing this value with the theoretical residence time ($\bar{\tau}$):

$$\bar{\tau} = \frac{\varepsilon V_r}{Q} \tag{16}$$

Where ε is the total porosity of the packing material, V_r is the volume of the empty column, and Q is the volumetric gas flow. When $t_m > \bar{\tau}$, the flow is bypassing or channeling.

The second moment of the RTD is described by the variance function σ, which is calculated from Eq. (17):

$$\sigma^2 = \int_0^\infty (t - t_m)^2 E(t)\, dt \tag{17}$$

The magnitude of this moment represents the degree of deviation of the flow from the plug flow behavior. This value corresponds to the distribution amplitude, where higher values result in a high deviation from plug flow, and lower values signify less intermixing effects (Bérard et al., 2020).

Additionally, the normalized RTD function is frequently used to compare the flow performance between reactors of different sizes (Fogler, 2006) and is given by Eq. (18) and Eq. (19):

$$E(\theta) = t_m E(t) \tag{18}$$

$$\theta = \frac{t}{t_m} \tag{19}$$

The parameter θ represents the number of reactor volumes of fluid that have flowed through the reactor at a given operational condition.

The normalized variance σ_θ is a parameter used to measure the spread of the flow distribution. The resulting value indicates if the reactor behaves as a plug flow (value near zero) or a perfectly mixed (value near to one) reactor (Gao et al., 2020) and is obtained from Eq. (20):

$$\sigma_\theta{}^2 = \frac{\sigma^2}{t_m{}^2} \tag{20}$$

The amount of injected tracer M_0 (g) can be obtained from the following relation:

$$M_0 = \int_0^\infty QC(t)\, dt \tag{21}$$

Where Q is the volumetric gas flow rate, which is usually constant.

Finally, the Peclet number Pe of the reactor is obtained from the dimensionless axial dispersion model in closed vessels, which is obtained by the mass balance of the tracer defined by Eq. (22):

$$\frac{\partial C}{\partial \theta} = \frac{1}{Pe}\frac{\partial^2 C}{\partial z^2} - \frac{\partial C}{\partial z} \tag{22}$$

Where z is the dimensionless length.

The solution of this equation is obtained considering an impulse input at $z = 0$ approximated by a fast exponential with the Danckwerts boundary conditions to account for the axial dispersion effects at the inlet and outlet of the biofilter (Zarook et al., 1998):

$$E(t) = C(z = 1, t) \tag{23}$$

$$C_{in} = C|_{z=0} - \frac{1}{Pe}\left.\frac{\partial C}{\partial z}\right|_{z=0} \tag{24}$$

$$\frac{\partial C}{\partial z} = 0, z = 1 \tag{25}$$

With the initial conditions of $C = 0$ at $t = 0$.

3.4 MASS TRANSFER COEFFICIENT ESTIMATION

The oxygen mass transfer inside the abiotic packed bed column was characterized by the well-defined chemical reaction of the sodium sulfite oxidation method (Cooper et al., 1944;

Kensy et al., 2005; Lo et al., 2001). Experiments were performed in an externally stirred tank reactor with a volume of 1.2 L connected to the packed bed column (see Figure 7). The stirred tank was loaded with 1.2 L of 0.07 M Na_2SO_3 solution was continuously agitated at 200 rpm while the solution was recycled into the column at a flow rate of 400 mL min^{-1} into the top using a peristaltic 520-S pump (Watson Marlow, UK). The liquid phase occupied almost the entire tank volume and was sealed to ensure oxygen transfer inside the column. The packed bed operated counter-current with an inlet airflow of 8 L min^{-1} measured with a variable-area rotameter V series (Aalborg, USA). Before the mass transfer measurements, the reactor containing the Na_2SO_3 solution was operated in countercurrent for about 10 minutes until the solution was saturated and the flows stabilized inside the column (Quijano et al., 2009). Later, 5 mL of a 0.368 g mL^{-1} $CoSO_4$ catalyst solution was added to the stirred tank, and aqueous samples of 5 mL were drawn from the bulk phase of the stirred tank reactor in time lapses of 1-2 minutes, starting from the catalyst injection time for a total reaction time of about 20 min Finally, the SO^{-3} concentration was determined by iodometric back-titration with a solution of 0.05M $Na_2S_2O_3 \cdot 5H_2O$ at 20 C as titrator (Appendix I).

The $k_L a_{O_2}$ was determined according to (Muñoz et al., 2018) using Eq. (26)

$$k_L a_{O_2} = \frac{OTR}{\frac{C_{O_2,G}}{H_{O_2}} - C_{O_2,L}} \tag{26}$$

Where OTR is the oxygen transfer rate, and is calculated from the slope of the absorbed O_2 concentration (estimated from the SO_3^{-2} concentration multiplied by the O_2/SO_3^{-2} stoichiometric coefficient derived from Eq. 26) versus time plot, H_{O_2} stands for the dimensionless Henry law constant of O_2 and $C_{O_2,g}$ represents the oxygen concentration in the exhaust gas.

The toluene volumetric mass transfer coefficient ($k_L a_{tol}$) was estimated from the $k_L a_{O_2}$ according to the following relation for perfectly mixed systems:

$$k_L a \approx \left(1/V_m\right)^{0.4} \tag{27}$$

This equation estimates the mass transfer coefficient across an aqueous phase as a function of its molecular volume at the boiling point (V_m). In addition, Muñoz et al. (2018)

demonstrated that the mass transfer from a given substrate could be estimated from a reference gas if the operational conditions and the reactor are the same using the following equation:

$$\frac{k_L a_{tol}}{k_L a_{O_2}} = \frac{\left(1/V_{m,tol}\right)^{0.4}}{\left(1/V_{m,O_2}\right)^{0.4}} \quad (28)$$

Where the used values of $V_{m,tol}$ and V_{m,O_2} used for $k_L a_{tol}$ estimations were 25.6 and 106.3, respectively (Estrada et al., 2014).

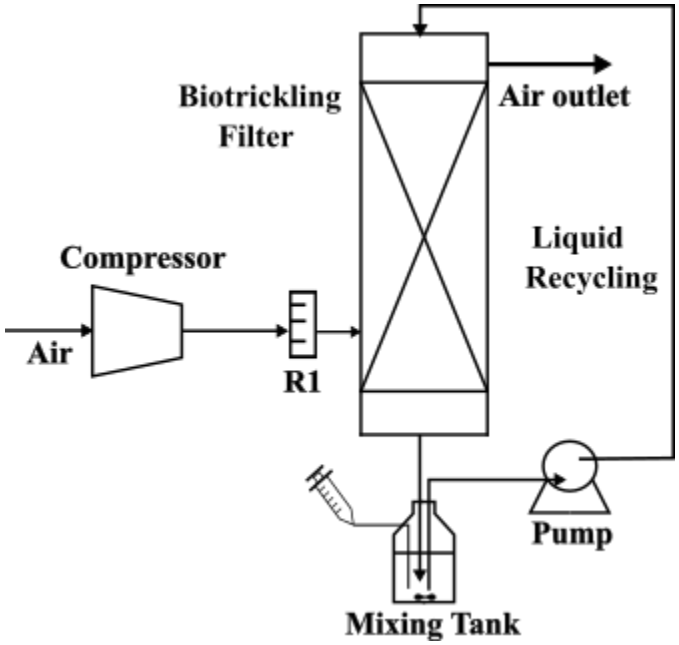

Figure 7. **Schematic representation of the experimental setup used to determine the gas residence time distribution.**

3.5 COMPUTATIONAL TOMOGRAPHY OF THE PACKED BED COLUMN

The computational tomography technique was used to obtain a 3D realistic description of the porous zone. CT imaging was applied over the column structure after the RTD and mass transfer coefficient estimations, to ensure that the porous distribution stayed invariable

between the experiments and the imaging procedure. Firstly, the whole structure was carefully unmounted and separated from all metal parts to avoid image distortions. Secondly, the column was translated to the "Clínica Universidad de Los Andes" for the image reconstruction procedure. The computerized tomography was applied using a Phillips PET/CT Digital Vereos scanner, with a maximum resolution of under 1 mm. Next, the 3D reconstruction was carried out by interpolating two contiguous images in DICOM file format using the open-source software 3D Slicer. This software allowed us to scale, modify the orientation and filter the column from the porous zone. The region of interest was filtered by applying different thresholds based on density. The resulting image was exported in STL (STereoLitography) format. Finally, postprocessing was done using the open-source software MeshLab to ensure that the file vectors were consistent with the experimental porous distribution.

3.6 BIOFILM IMAGING INSIDE A BIOTRICKLING FILTER

3.6.1 Description of the system

A biotrickling filter reactor was developed as a research tool to analyze the feasibility of applying contrast CT imaging as a methodology to understand the influence of the gas and liquid flows over the local biofilm formation. The reactor setup was a modified version used for the RTD and the mass transfer coefficient estimation experiences. The gas inlet flow was obtained through an air compressor divided into two streams: one flowing to a humidification column and the other flowing to a gas generator. The gas generator consisted of the evaporation of toluene by bubbling, and the gas flow used to generate the polluted gas was controlled by a mass flow controller (Colepalmer, EW-32907-69, IL, USA). Subsequently, the air-toluene stream was mixed with the humidified air inside a mixing chamber before entering the reactor. Two sampling ports for the gas measurements were used, consisting of an IPB type T connector (Taylor Automatizacion, Chile) capped with a butyl septum were placed at 0.06 cm from the inlet and outlet of the column. The mass controller flow rate was used to adjust the inlet concentration of toluene inside the column. The concentration of toluene in the gas phase was measured from these ports using an FID-GC (Shimadzu 2014 chromatograph) with a DB-264 column at 260°C with a retention time of 3 minutes using helium as a carrier with a flow rate of 5 mL min^{-1}. The liquid phase was recycled from a 2.2

L external holding tank using a peristaltic pump. The detailed diagram of the experimental setup is shown in Figure 8. *Pseudomonas Putida* F1(*PpF1*) strain (DSMZ 6899) and toluene were chosen as the inoculum and model VOC, respectively. The latter criteria was selected for the present work due to its high maximum specific growth rate ($\mu_{max} = 0.78\ h^{-1}$), which reduced the inoculum cultivation period and allowed to focus this study only on the mass transfer limitations rather than on biodegradation kinetics The mineral salt medium used for bacterial cultivation was the mineral medium Brunner (MMB) with composition (g L^{-1}): $Na_2HPO_4 \cdot 7H_2O$, 4.9; KH_2PO_4, 1.52: $(NH_4)_2SO_4$, 1; $MgSO_4 \cdot 7H_2O$, 0.2; $CaCl_2$, 0.038; and 10 mL L^{-1} of trace element solution containing (g L^{-1}): EDTA, 0.5; $FeSO_4 \cdot 7H_2O$, 0.2; ZnSO4 · 7H2O, 0.01; $MnCl_2 \cdot 4H_2O$, 0.003; H_3BO_3, 0.03; $CoCl_2 \cdot 6H_2O$, 0.02; $CuCl_2 \cdot 2H_2O$, 0.001; $NiCl_2 \cdot 6H_2O$, 0.002; $NaMoO_4 \cdot 2H_2O$, 0.003. The final pH of the medium was 7.0 pH.

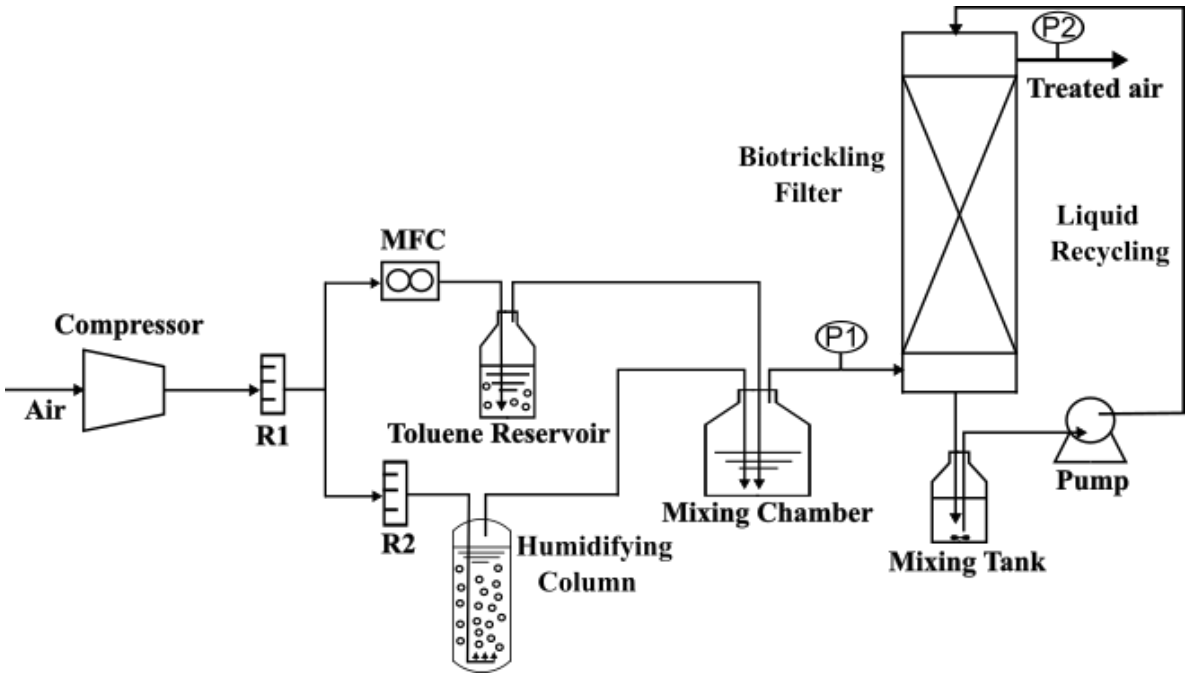

Figure 8. **Schematic representation of the experimental set-up used in the biofilm formation**. MFC: mass flow controller; R1: Rotameter 1; R2: Rotameter 2; P1: inlet gas sampling port; P2: outlet gas sampling port.

3.6.2 Abiotic losses and system maintenance.

The system was tested for abiotic toluene losses to ensure that the variation in concentrations was due to biodegradation. Firstly, with all the valves closed, the whole column volume was filled with water for 24 hours to guarantee the system was free of water leaks. Secondly, the gas leak was evaluated by monitoring the gas inlet and outlet concentration operating with a gas flow of 8 L min^{-1} with a constant inlet concentration of 1 g m^{-3} of toluene until the inlet and outlet concentration differences were negligible. Finally, the system was operated with an airflow of 8 L min^{-1} and a TLV of 2 m h^{-1} for seven days to ensure the system could operate without interruption. Additionally, to ensure the operation's proper maintenance, the water inside the humidifying column was changed every week. The temperature inside the laboratory was controlled using a microcomputer temperature controller ETC-974 (VETO, Chile) connected to a fan heater, and the moisture from the compressor was drained every two days of operation.

3.6.3 Biotrickling filter start-up and operation.

To furnish fresh inoculum, 1.5 mL of *PpF1* bacteria in stock (stored at -20°C) was incubated for 12 hours in 50 mL E-flasks supplied with 30 mL of nutrient broth in an orbital shaker at 200 rpm and 30°C. Then, the 30 mL of fresh inoculum was transferred into a 250 mL E-flask containing 200 mL of MMB, and 250 µL of toluene was supplied inside the flask, closed with cotton plugs, sealed with aluminium and parafilm to avoid the leak of toluene, and incubated in the orbital shaker for 12 hours. Finally, 400 mL (two E-flasks cultivated in parallel) were added to 1.6 L of MMB and supplied into the external tank of the biotrickling filter. The initial concentration of inoculum inside the stirred tank reactor was approximately 6.22 g L^{-1}. The inoculum accumulated inside the external tank was recirculated back into the bed at a TLV of 2 m h^{-1}. The BTF was acclimated using an inlet load rate of 67-70 g m^{-3} h^{-1} for two weeks, with an EBRT of 48 s and a constant stirrer speed of 200 rpm. The MMB renewal maintained the pH at a constant value of 7 during the operation, with a renewal rate of 200 mL of culture medium with fresh MMB daily. The system's temperature was controlled and held steady at 25°C using a fan heater connected to a temperature microcontroller. The operational conditions of the system were maintained constant for 70 days until a steady state was achieved.

3.6.4 Maximum elimination capacity of toluene at constant EBRT under steady state

The influence of the toluene inlet load on the elimination capacity (EC) of the BTF was performed after the acclimation period. This experience was assessed by increasing the toluene concentration of 0.655 to 1.830, 2.225, and 2.757 g m^{-3} at a constant EBRT of 48 s, corresponding to loading rates of 67.39 to 160.91, 236.21, and 259.34 g m^{-3} h^{-1}, respectively. The inoculum accumulated inside the external tank was recirculated back into the bed at a TLV of 2 m h^{-}1. The MMB renewal maintained the pH at a constant value of 7 during the operation, with a renewal rate of 200 mL of culture medium with fresh MMB daily. The system's temperature was controlled and held steady at 25°C using a fan heater connected to a temperature microcontroller.

3.6.5 Assessment of the biofilm formation by contrast computational tomography

A computational contrast tomography was applied using a 0.35 g mL^{-1} suspension of barium sulfate 95% (Eskay Speciality Chemicals, India) over the BTF at a steady state operating under the maximum elimination capacity. The solution was prepared in 800 mL of MMB and introduced into the external stirred tank reactor to be recirculated at a constant TLV of 2 m h^{-1} for 2 hours. This velocity was the same used for the experience, and as the velocity was laminar, their effect on the biofilm detachment has been neglected for this study. The scanner properties and image recovery protocol were described in section 3.1.3.

3.7 CFD SIMULATIONS

The computation of the velocity field and RTD from the simulation inside a realistic description of the packed column was implemented in the open-source CFD software OpenFOAM (Weller et al., 1998). The simulations and mesh generations were run in parallel in 4 cores.

3.7.1 Computational domain

The 3D geometry of the fluid inside the empty column was modeled to generate the computational domain where the transport equations were solved. The process was done

using the Salome-Meca software to generate a closed manifold surface of the fluid field, based on the column dimensions, and define the region names.

3.7.2 Mesh generation

The automated meshing utility *cfMesh* (Juretic, 2017) was used to create a hexahedral mesh from the geometry. First, the resulting STL file extension (*.stl*) obtained from Salome-Meca was exported into an FMS file format (*.fms*), as suggested by the *cfMesh* developer. This was done to ensure that the complete information about the feature edges and patches of the geometry was considered in the mesh generation. Secondly, the porous zone was generated into the fluid domain using the OpenFOAM utility *snappyHexMesh* by snapping the surface information inside the STL file obtained from the scanner. This utility generated porous walls inside the column based on castellated irregular-shaped mesh cells. Later, the *checkMesh* utility was used to perform the mesh validation.

3.7.3 *simpleFoam* solver

The OpenFOAM solver *simpleFoam*, based on the Semi-Implicit Method for Pressure-Linked Equations (SIMPLE) algorithm, was used to simulate the gas pressure and velocity fields inside the packed column. The flow and mixing of incompressible and Newtonian fluids under isothermal conditions are governed by fundamental conservation equations for mass, given by Eq. (28), and momentum, described by the Navier-Stokes equation (Bird et al., 2006), given by Eq. (29):

$$\nabla \cdot \vec{u} = 0 \tag{28}$$

$$\frac{\partial \vec{u}}{\partial t} + (\vec{u} \cdot \nabla)\vec{u} = -\frac{1}{\rho}\nabla P + \nu \nabla^2 \vec{u} \tag{29}$$

Where $\vec{u}$ represents the velocity vector, P the pressure, ρ the fluid density, ν the kinematic viscosity of the fluid, and t the time.

3.7.4 *scalarTransportFoam* solver

The OpenFOAM solver *scalarTransportFoam* was used to simulate the tracer injection. The dynamic flow simulation was solved based on the velocity field obtained in the fluid simulation after reaching a steady state. In this way, the RTD was computed by solving the passive scalar transport equation:

$$\frac{\partial \mathrm{T}}{\partial t} + \vec{u} \cdot \nabla \mathrm{T} = \mathcal{D} \cdot \nabla^2 \mathrm{T} \tag{30}$$

Where, T is the tracer concentration treated as a passive scalar, and $\mathcal{D}$ is the tracer diffusion coefficient.

3.7.5 *interFoam* solver

The trickling bed simulation was carried out by using the solver *interFoam* based on a volume of fluid (VOF) approach for two-phase flows. This solver considers both phases as only one fluid with fast changes in fluid properties. Therefore, one set of Navier-Stokes equations is solved. The phases are distinguished by adding a transport equation for the volume fraction which tracks the distribution of the phases through the computational domain. The Navier-Stokes and continuity equations are solved by applying the Pressure-Implicit with Splitting of Operators (PISO) algorithm, while the interphase is calculated with the *interFoam* application by solving the Navier-Stokes equations with an additional indicator function:

$$\frac{\partial \alpha}{\partial t} + \nabla \cdot \alpha \vec{u} + \nabla \cdot (\alpha(1-\alpha)\vec{u}_c) = 0 \tag{31}$$

From Eq 31, α represents the VOF indication function, which defines the quantity of liquid phase per unit of volume at each computational cell (i.e., if $\alpha = 1$, the cell contains only liquid, if $0 < \alpha < 1$, the cell contains a mixture of both phases, and if $\alpha = 0$ the cell contains only gas). Additionally, the term $\vec{u}_c$ represents the convenient velocity field to compress the gas-liquid interphase. Both fluids were considered Newtonian, incompressible, isothermal, and immiscible. (Moreno-Casas, 2020b).

3.7.6 Gas flow simulation.

The *simpleFoam* solver presented in section 3.7.3 was used to simulate the gas velocity and pressure fields inside the packed column. The assumptions described in (Moreno-Casas et al,

2020) were applied to model the behavior of the fluid as an incompressible fluid whose density and fluid properties were constant during the simulation period. The flow regime inside the porous zone was established by applying the pellet Reynolds number (Moghaddam et al., 2020) defined by Eq. (32) and Eq. (33):

$$Re_p = \frac{\rho u_y d_{pv}}{\mu} \tag{32}$$

$$d_{pv} = \sqrt[3]{1.5h(d_o^2 - d_i^2)} \tag{33}$$

Where, u_y represents the averaged velocity in the y-direction, d_{pv} denotes the diameter of a sphere of equal volume, h represents the height of one ring, and d_o and d_i represent the outer and internal diameters of each ring, respectively. The fluid properties were assumed to be air at the operational conditions (density value of 1.1115 kg m^{-3} and dynamic viscosity of $1.8 \cdot 10^{-5}$ Pa s).

Later, the tracer injection was simulated over the converged velocity vectors using the *scalarTransportFoam* solver. The diffusion coefficient $\mathcal{D}$ for butane into the air, was calculated by applying the Chapman and Enskog correlation (Poling et al., 2004) with a value of $1.066 \cdot 10^{-5}$ m^2 s^{-1}. This transient computation was carried out with a computational time of approximately five times the empty bed residence time of the gas in the column, with a constant time step of 0.01 s. Second-order discretization schemes were used for the simulation with a residual value of 10^{-5}. The injection signal was simulated as a simple square signal because of its simplicity. A summary of the initial and boundary conditions, discretization schemes, and solvers used for both simulations is given in the supplementary section.

3.7.7 Liquid flow simulation.

The *simpleFoam* solver presented in section 3.7.3 was used to simulate the liquid velocity and pressure fields inside the packed column. The average liquid velocity inside the inlet tube of 0.0326 m s^{-1} was obtained from the relation between the volumetric flow rate (0.4 L min^{-1}) and the cross-sectional area of the tube in the flow direction ($1.767 \cdot 10^{-4}$ m^2). The fluid

properties were assumed to be those of water at the operational conditions (density value of 998.986 kg m^{-3} and dynamic viscosity of $1.02 \cdot 10^{-3}$ Pa s).

3.7.8 Gas-Liquid flow simulation.

The *interFoam* solver was used to obtain the gas-liquid interface inside the packed column. In order to approximate the steady state of the trickle bed, the OpenFOAM utility *mapFields* and *setFields* were applied to import the velocity field data obtained from the one-phase simulations inside the internal mesh as initial conditions. Second-order discretization schemes were used for the simulation with a residual value of 10^{-5}.

All the simulations, mesh generation, modeling, rendering, image processing, sensor measurements and data postprocessing were carried out using a laptop ASUS ROG GL553VE Intel ® Core™ i7-770HQ CPU @ 2.80GHz x 8 with a graphic card NVIDIA GTX 1050 Ti (2018).

4 RESULTS AND DISCUSSIONS

Some of the results presented in this section were published in the following paper, "A convenient method to validate the gas flow of a CFD-CT simulation applied on a packed bed used in gas biofiltration through residence time distributions" with DOI:

https://doi.org/10.1016/j.cej.2022.138795

4.1 SENSOR IMPLEMENTATION

The implementation of the MOx sensor requires the determination of the time constants to filters the transient behavior of the signal. These time constants were obtained from 20 different concentration steps in a range between 0.299 and 2.88 V, where 2.88 V represents the saturation voltage of the sensor. An almost instant response time constant was found for the rising phase. Indeed, the minimum and maximum response times recorded were 0.03 and 0.077 s for a step change at 0.299 and 2.88 V, respectively. The slight fluctuations in the first few data points (Figure 9) were likely caused by the sensor movement when the syringe needle contacted the sensor's surface. Nevertheless, this effect on the calculations of the time constants was negligible. The rise phase time constant was set to zero as the values obtained

were close to the data acquisition rate of 0.05 s. The calculated recovery time constants accounted for 0.1 and 0.69 s for a step change of 0.299 and 2.88 V, respectively. These values resulted in a response faster than expected and were probably due to the high reaction rate between the oxygen and the sensor surface caused by the application of the constant airflow. This phenomenon resulted in a faster resistance increase, thus accelerating the recovery from the transient sensor behavior. Therefore, the recovery time constant was computed from the mean of the four values obtained near saturation. To simplify the sensor model, the resulting average τ_d of 0.622 s was set as the constant for all concentrations due to the insignificant difference between the minimum and maximum values.

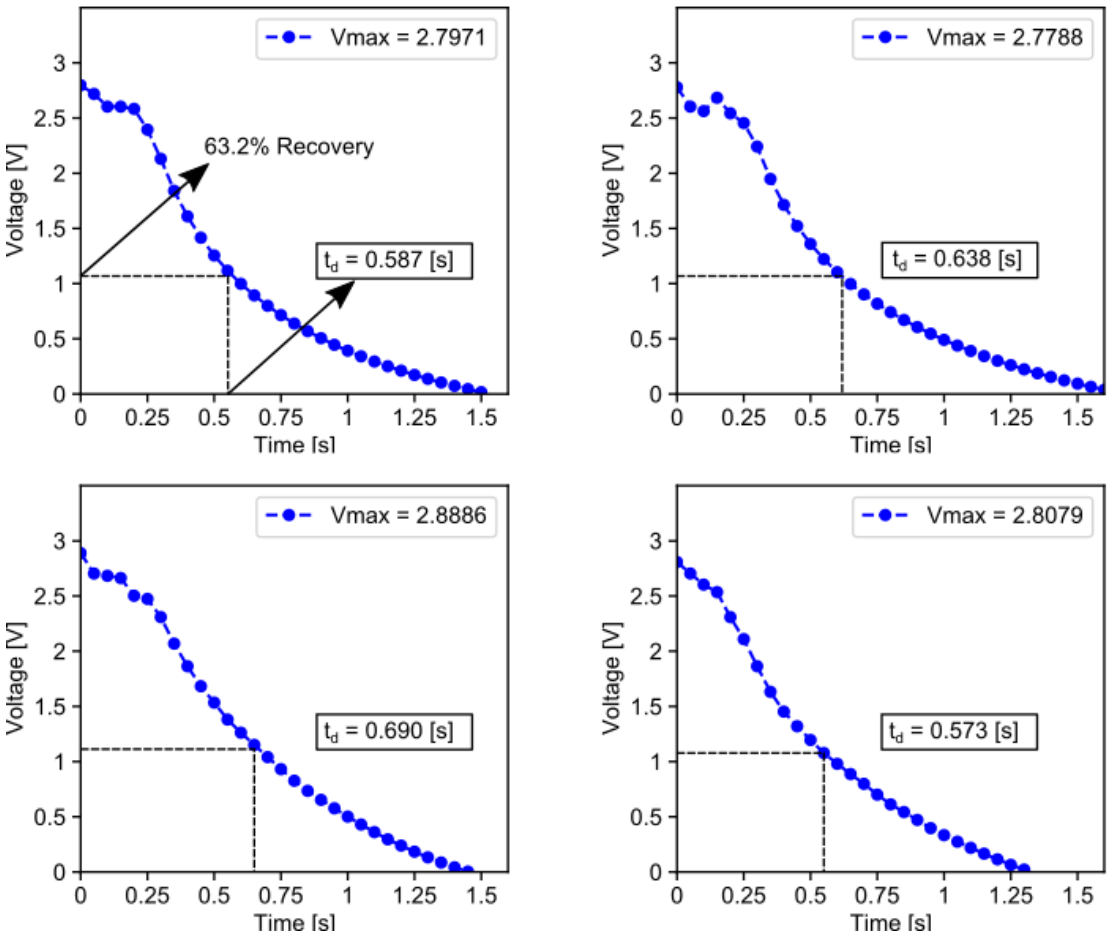

Figure 9. **Determination of the decay phase time constant from four random steps stimulus near the saturation.**

4.2 MESH GENERATION.

4.2.1 Porous bed image reconstruction

Figure 10 shows the 3D representation of the sequence of 1126 2D images in DICOM format obtained from the CT scan. The figure (left) shows the reconstruction of the image of the reactor, where the inlet and outlet pipes are connected to the cylindric reactor walls. On the right of the figure, the porous media composed by polybutylene rings can be depicted. In this last image the top and bottom flanges are visible, as well as the location of the inlet and outlet pipes, showing their position with respect to the porous structure.

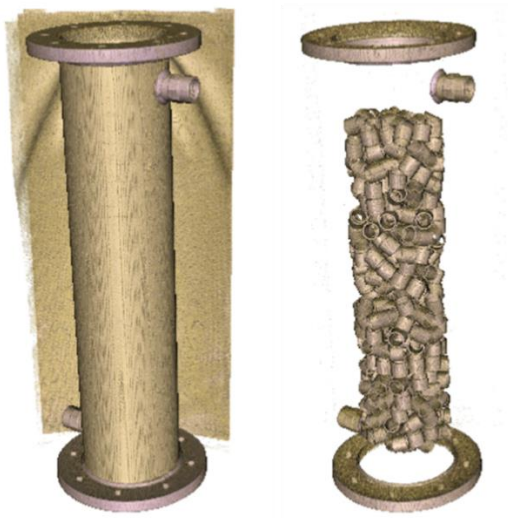

Figure 10. Computational tomography of the polybutylene rings structure.

The reactor and its porous 3D structure shown in Figure 10, has been generated by reconstruction from 2D images (Figure 11). Care must be taken in the reconstruction as the images must be scaled and oriented at the same operation angle as the experiments. However, the CT procedure required to place the column horizontally over a protection cloak which altered the image reconstruction angle (Figure 11, panel A). Thus, the orientation repair was achieved using a B-spline interpolation to transform the information stored in the nodes that define the position and orientation of the volume in the coordinate system. The matrix transform was obtained considering that both flanges were parallel to the x-axis. This inclination was verified experimentally using an inclinometer to ensure the column was aligned with the structure. The nonparametric and unsupervised method of an automatic threshold intensity range for picture segmentation proposed by Otsu (1979) was used to segment the porous zone from the flanges due to its simplicity. The air was filtered from the

image by masking the threshold range between -1024.00 and -500, and the porous structure was segmented using the threshold range between 600 to 3070.98 (Figure 11, panel B). Rezaei et al. (2019) also concluded that this method was the best algorithm for segmenting porous carbonates, although the threshold methods' sensitivity might result in reconstruction errors, and contrast agents may be required. In this study, the packing material opacity allowed us to easily filter the polybutylene rings from the methacrylate walls, as the difference between the thresholds was large enough to clearly differentiate both segments.

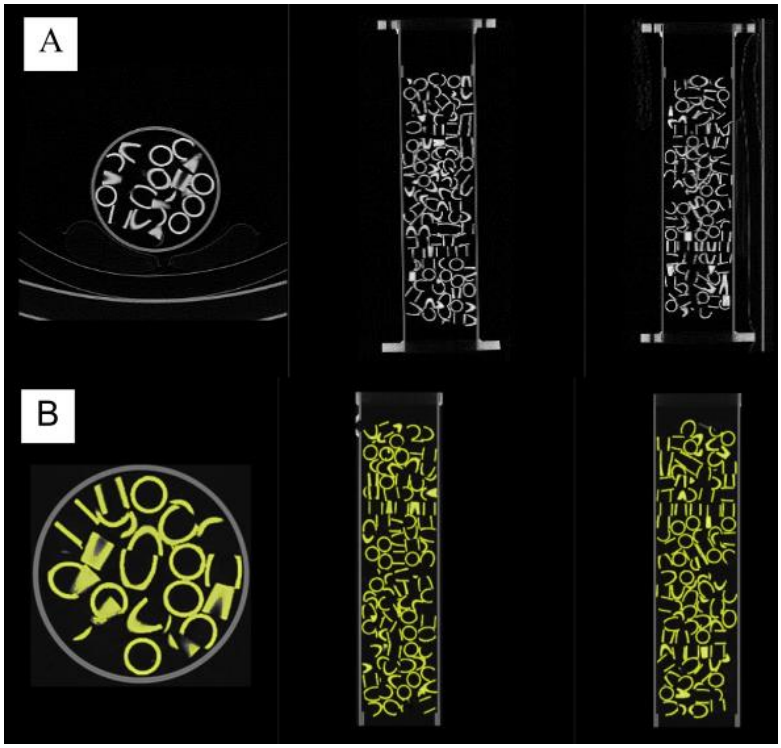

Figure 11. **Axial, coronal, and sagittal slice orientation of the packed bed column**. (A) Raw DICOM file (B) Oriented and segmented image.

However, to avoid pixel losses from the Otsu method, the fast GrowCut method proposed by Zhu et al. (2014) was used to improve the pixel capture and adequately capture the porous zone. This was done using the ring threshold segmentation as the master volume and filling the neighboring pixels of the region of interest by masking the air phase. The resulting file consisted of 9795010 faces and 4894894 vertices to guarantee a realistic structure description (Figure 12). Finally, the porosity was measured by volume difference resulting in a value of 0.9013, almost the same as the one obtained experimentally (0.90). Thus, it seems reasonable

to state that the image reconstruction can represent a realistic description of the porous zone.

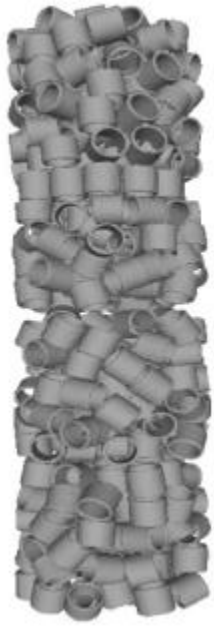

Figure 12. **Reconstructed realistic description of the porous zone as .stl file.**

4.2.2 Empty bed Mesh

Figure 13 shows the computational domain of the empty tubular reactor used in the simulations. The gas inlet and outlet primitive data type of the *fms* file were set as *patch* for the gas phase and multiphase simulations and as *wall* for the liquid phase simulation. Similarly, the gas inlet and outlet primitive type was set as *patch* for, the gas phase and multiphase simulations and as *wall* for the liquid phase simulation. These data types allows the proper boundary recognition to the code. This fluid domain was employed as the vectorization template.

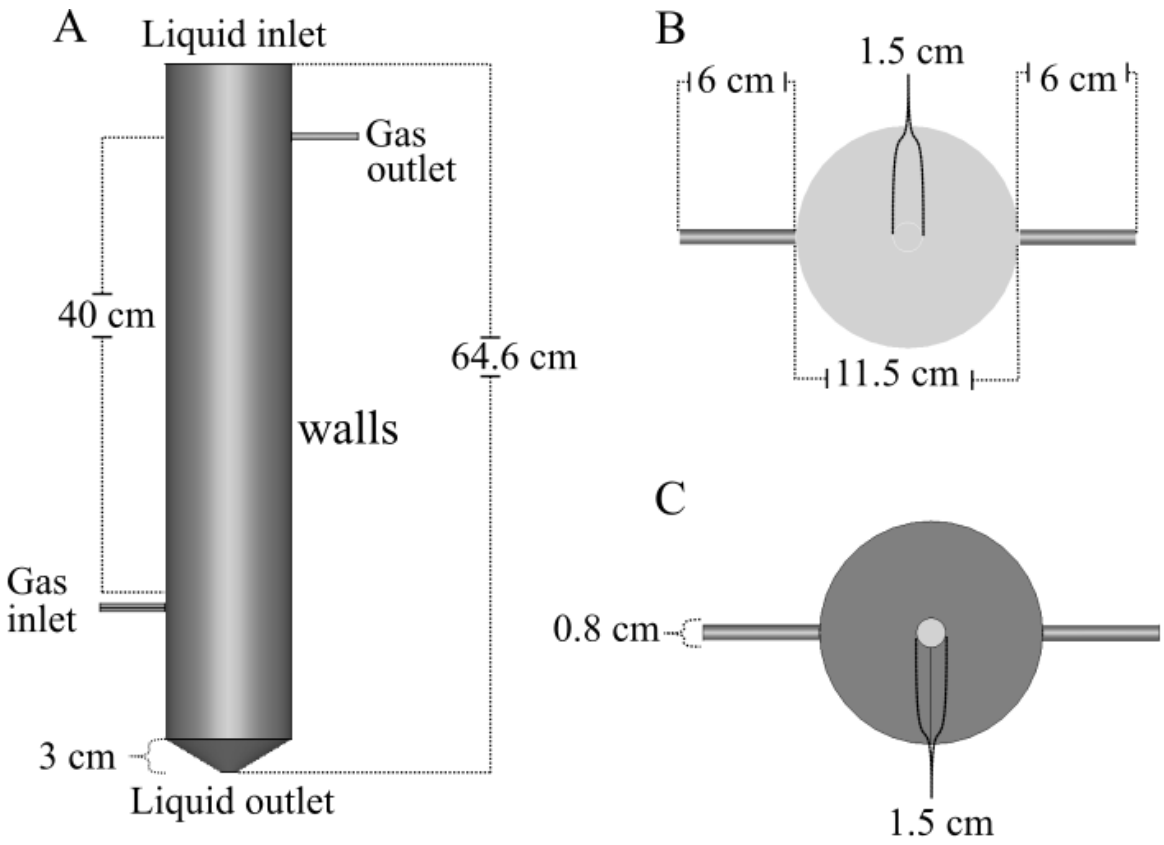

Figure 13. **3D fluid computational domain.** (A) Frontal, (B) Top, and (C) Bottom view

The fluid domain mesh was generated before snapping the porous zone. Then, the quality of the mesh was evaluated in terms of non-orthogonality, aspect ratio, and skewness. As a result of the mesh sensitivity analysis (described in Section 4.3), the selected mesh consisted of 6.9 million cells (99% hexahedra) with an average non-orthogonality of 1.794 for the empty bed domain. Consequently, the snapped porous zone consisted of 6.3 million cells (94% hexahedra) with an average non-orthogonality of 4.804, a maximum aspect ratio of 9.019, and a maximum skewness of 5.961. Skewness values close to zero are expected to ensure good mesh quality (Sadino-Riquelme et al., 2018). However, the number of elements with found with high skewness is negligible compared to the whole mesh. The meshing procedure took about 21 minutes to compute the mesh.

4.3 GAS FLOW CHARACTERIZATION

The validation of 3D CFD modeling is critical when used as a tool for designing gas biofiltration units. 3D CFD can become an important for understanding and improving the design and operation of biofilters and the engineering of new packing media. The simulation results of CFD models can be analyzed in detail to understand the flow behavior at any location of the biofilter at any simulated time, a characteristic that conventional RTD models do not allow. Nonetheless, model validation can be achieved by comparing the numerically obtained RTD with the experimental results of the moments of the RTD function. The latter is what has been done in the present study.

4.3.1 Experimental RTD of the gas phase

After initializing the sensor, the first measurement of butane in the outlet stream was detected after 35.377, 35.429, and 35.478 s for each experience (triplicate). Since each pulse was executed approximately 30 seconds after initializing the sensor, the mean time between the injection and the first signal was 5.428 ± 0.05 s. The low standard deviation among these results, which is the same value as the data acquisition rate, confirmed the representativeness of the pulse injection protocol. The results obtained from the triplicate experiments are shown in Figure 14, panel A. The mean signal peak value accounted for 2.367 ± 0.027 V and was obtained at 31.892 ± 0.361 s after the injection of the butane pulse. The voltage data range remained below saturation, suggesting that the 10 mL of pure butane injected was enough to capture the concentration profile without inducing tracer measurement losses from concentrations higher than the sensitivity range. This injection corresponds to 0.170% of the gas volume inside the reactor, ensuring that the pulse injection had a small tracer volume. In each test, the syringe needle was carefully injected through the septum and placed in the middle point of the pipeline to avoid dead volumes inside the glass tube. The pulse method requires a small tracer volume injected in the reactor that must mimic a Dirac delta function (Nauman, 2008). Thus, the injection time was carried out as fast as possible to ensure times under one second, which is below 2.4% of the reactor mean residence time. A polynomial regression (9^{th} degree, with an R^2=0.999) was generated from the raw data to represent the average experimental flow behavior values. This model started after a time delay of 5.428 s to emulate the behavior of the triplicates. This regression model was then filtered from the

transient behavior using Eq. (12-13) with the set recovery time constant of 0.622 s (Figure 14, panel B). The negligible difference between the regression model and the filtered curve results from the flow effect over the sensor recovery. From the calibration, the R_0 value of 18 kΩ, was obtained and used to estimate the concentration of butane at the reactor outlet. This value was slightly higher than the range between 5~15 kΩ provided by the manufacturer since the load resistor used in these experiments was 10 kΩ (compared to the 4 kΩ used by the manufacturer), and our calibration process did not consider the effect of humidity in the results, nevertheless, this result was acceptable for MOx sensors under similar conditions (Dorcea et al., 2019). The resistance was then calculated from Eq. (12), and the outlet concentration was measured using the sensitivity curve provided by the manufacturer (Appendix A1). The initial mass recovered from the sensor measurements was calculated by using Eq. (21) between the initial and final time of the experience, resulting in 19.38 mg, compared to 23.21 mg present in the 10 mL pulse of gas butane, which results in 83.49% of gas tracer recovery. The injected mass was estimated using the ideal gas law at the operational conditions. However, some values were estimated below 500 ppm (Figure 14, panel C), and their quantification could be erroneous. Therefore, the mass recovered was evaluated only on values over 500 ppm resulting in 16.276 mg or a 70.13% mass recovery. Additionally, if the rotameter flow rate calibration at standard conditions is considered, a 93.25% mass recovery could be achieved. Nevertheless, and as mentioned before, this quantification is also dependent on the proper calibration of the sensor under different conditions of humidity, temperature, and circuit configuration. Although a complete tracer recovery is always difficult to obtain, a mass recovery range between 70.13-83.49% seems acceptable, as a similar recovery in a gas phase RTD using methane as a tracer in a fungal biofilter has been reported in the literature (Prenafeta-Boldú et al., 2008). The calibration effects under different operational conditions were neglected in this study as this is the first approach to this methodology. Consequently, the proper sensor feasibility was evaluated based on the RTD moments obtained from the signal measurements.

The theoretical RTD for the empty reactor and the packed column at the operational conditions were 48 and 44s, respectively. The mean RTD computed from the sensor measurements was obtained from the integral of the curve $E(t)$ (Figure 14, panel D) with a value of 41.89 s, with a relative difference of 14.314% and 5.021% when compared to the

empty bed mean RTD and packed bed RTD, respectively. The difference between both measurements highlighted the relevance of considering the effect of the porosity in the design of these columns. Additionally, the axial dispersion model obtained from the experimental data showed a coefficient of determination of 0.992, resulting in a Peclet number of 8.07. The normalized variance obtained experimentally was 0.220, which is not small enough to confirm that the flow regime inside the packed bed was close to a plug flow. This value was similar to the range of values (0.20-0.27) previously reported for biofilters in the literature (Zarook et al., 1998). In this context, materials with porosity values near one are prone to lower errors as their mean RTD is closer to the EBRT, hence the other RTD moments should be analyzed.

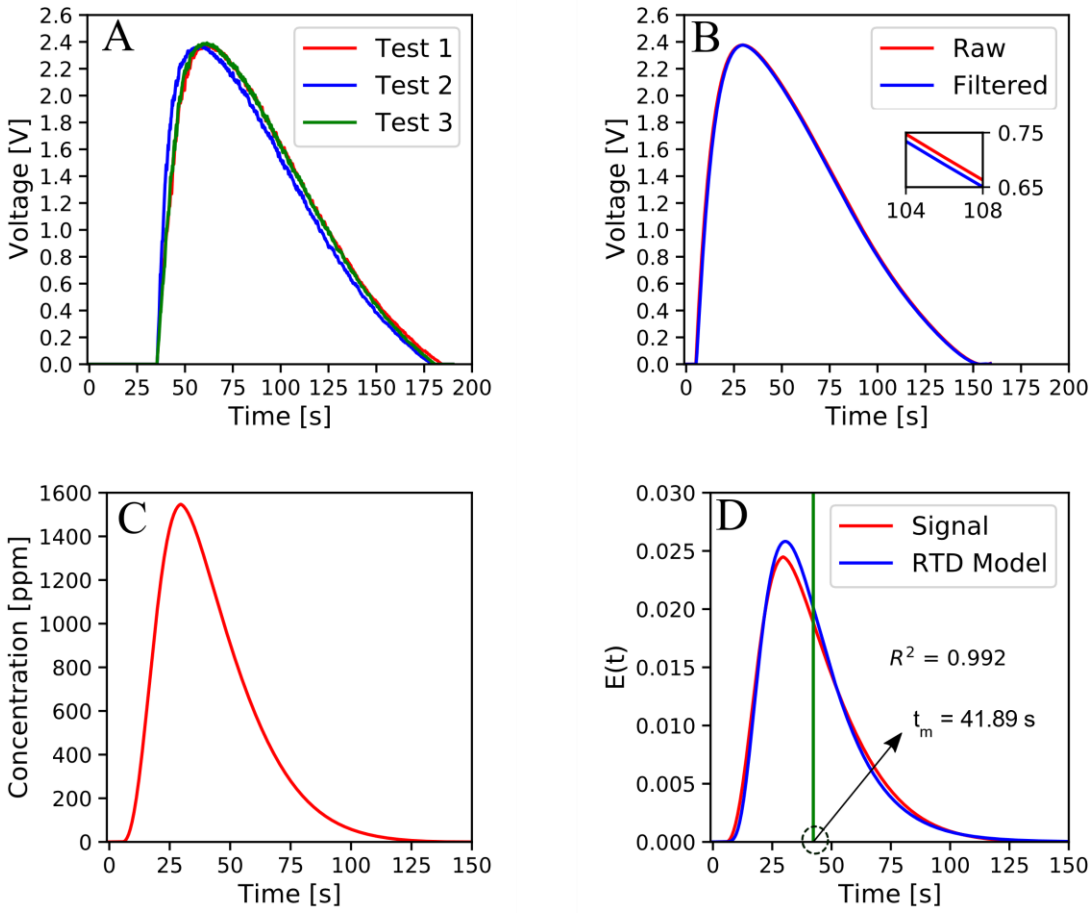

Figure 14. **Gas phase experimental RTD results.** Time course of the (A) raw voltage in triplicate experiments, (B) transient signal (red) compared with the steady-state signal (blue)

obtained from the sensor model, (C) butane gas concentration at the outlet of the column, and (D) experimental RTD function (red) compared with the axial dispersion model (blue).

4.3.2 Gas phase CFD simulation

First, the gas average velocity inside the inlet tube of 2.653 m s^{-1} was obtained by relating the volumetric flow rate (8 L min^{-1}) and the cross-sectional area of the tube ($5.027 \cdot 10^{-5}$ m^2) in the flow direction, resulting in a laminar regime as it contributes to a Reynolds number of 1311 < 2300. Later, by applying the equation of continuity at the end of the pipe (beginning of the column), an estimation of the average velocity inside the column was obtained for the cross-sectional area of the column (0.0103 m^2), resulting in a value of 0.0128 m s^{-1}. Thus, the flow regime was found to be laminar $\left(Re_p \approx 9.24\right)$ due to the low pellet Reynolds number. These values confirm that the flow is laminar in the whole structure, which validates the use of the *simpleFoam* solver (valid for incompressible and laminar flows).

Figure 15 compares the simulated tracer and the sensor's experimental measurements for the normalized (Figure 15, panel A) and cumulative (Figure 15, panel B) RTD functions. The implemented CFD model describes a similar behavior to that of the experimental RTD curve. The main differences between the curve shapes can be seen in the peak and the tail. This difference can be explained by the sensor's sensitivity to accurately measure concentrations outside its optimal detection range. This finding was consistent with the above-cited 83.49% mass recovery of the tracer. According to the results shown in the figures, the percentage of mass recovery seems to be enough to describe the right-hand side shape of the curve accurately and does not alter the final interpretation of the flow inside the column. Additionally, both cases predicted similar time convergence for the cumulative RTD function until a steady state was reached, and their difference in shape resulted from their different mean RTD value.

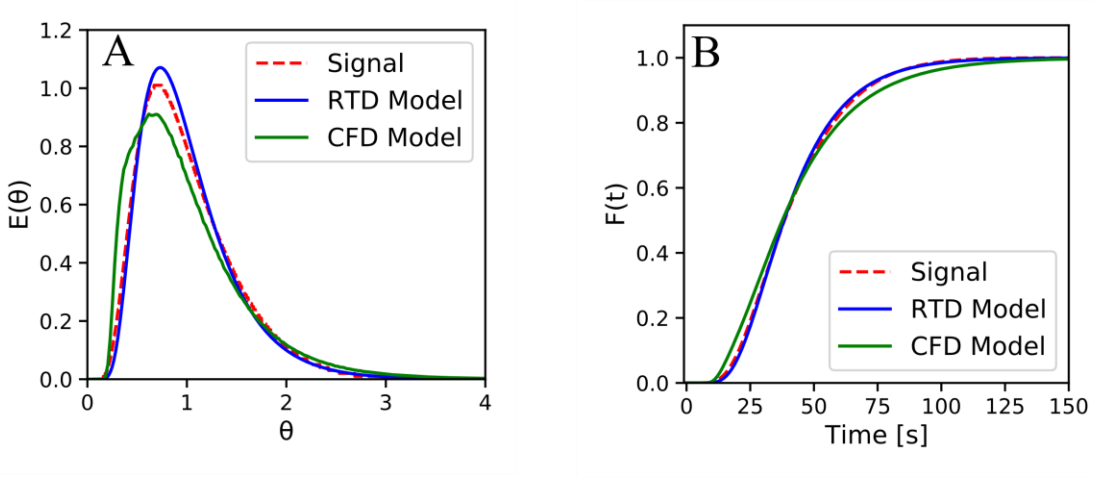

Figure 15. **Gas phase CFD validation through RTD**. The red line represents the experimental results, the blue line represents the axial dispersion model, and the green line represents the CFD model for (A) Normalized RTD function and (B) Cumulative RTD function.

The mean RTD and the normalized variance estimated in the simulation were 43.709 s and 0.326, respectively. Compared with the experimental results, a relative difference of 4.167% for the mean RTD and 32.515% for the normalized variance were found. In addition, butane was initially identified approximately five seconds after the simulation started, which matched the experimental observations. Therefore, these comparisons show that the CFD model employed herein is reliable enough to be use as a tool to explore, in detail, the mixing and flow behavior inside the biofilters packed bed.

Figure 16 shows the velocity iso-surfaces of the packed bed reactor obtained in the CFD 3D simulation. The differences in the gas velocity across the column show that mixing inside the reactor is not uniform (Figure 16, panel A). A poor gas distribution inside the packed bed can lead to non-uniform biofilm growth. A recirculation zone at the reactor entry (bottom) resulting from the flow spiralling up along the cylindrical wall is predicted by the simulation (Figure 16, panel B). This recirculation likely resulted in a delay in the tracer reaching the reactor outlet. At regions with low velocities, the tracer is trapped for a long time, much longer than the mean residence time. Eventually, all the tracer would reach out of the column by molecular diffusion, contributing to the tail of the RTD curve. Also, the packed bed simulation captured the preferential gas flow near the walls, as suggested by the higher gas velocities in those areas. This behavior occurs due to an inefficient configuration of the

packing material (near the walls), which could result in lower efficiencies in biofiltration systems due to the lower contact time between the pollutant-laden gas and the biofilm. Simulations validated with the procedure shown in the present study, should be able to identify gas circulation in the packed bed using CFD, which may help researchers and engineers understanding how new packing materials can be created to tackle improved performance of biofiltration units.

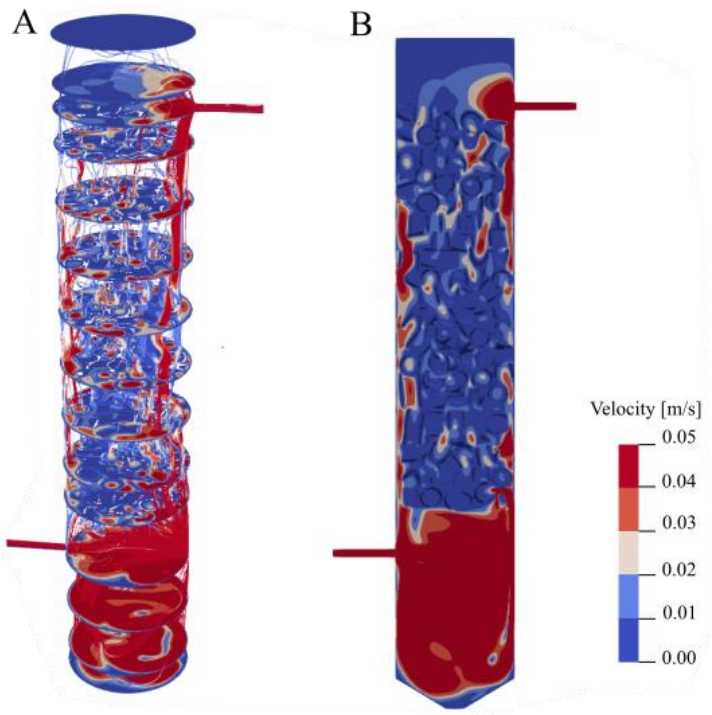

Figure 16. **Gas flow distribution inside the packed bed reactor**. (A) 3D representation of the velocity streamlines of the gas flow at different radial slices. (B) 2D slice representation of the velocity profile at the Z normal axis of the column. Near zero velocity zones (blue) indicate the presence of dead volumes where little or no gas movement occurs.

The smaller elements present in finer meshea can more accuratelly capture the cell data and results in more accurate results. Thus, a mesh independency study was carried out by repeating the simulation with a coarse mesh (Figure 17) and comparing it with a fine mesh to capture the mean RTD result with the maximum accuracy allowed by the mesh discretization. In this way, the mean RTD was 43.7097 s and 43.7102 s for the 6.3 million and 0.8 million cell meshes, respectively, with a difference is 0.001% between both simulations, confirming the mesh independency of the results.

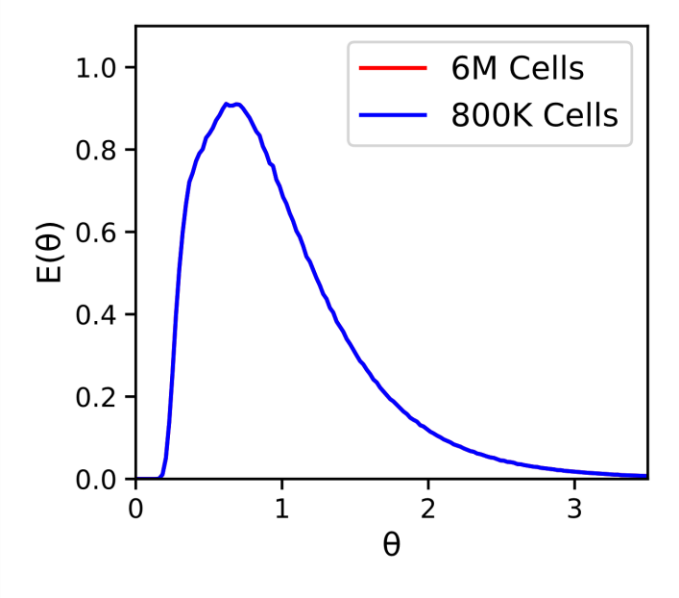

Figure 17. **Mesh independency study**. The blue line (0.8 million cells mesh) overlaps the red line (6.3 million cells mesh).

4.4 LIQUID FLOW CHARACTERIZATION

4.4.1 Experimental RTD of the liquid phase

The theoretical RTD measured for the packed column at the operational conditions assuming plug flow behavior was 14.5 min. However, due to the liquid flow maldistribution, the fluid does not flow through the whole packing material when moving towards the reactor outlet, resulting in less volume usage than the estimated theoretically. This is evident when comparing the mean RTD obtained experimentally, with a time of 6.485 s (Figure 18). This result is consistent with experimental results reported in literature operating under similar conditions (Trejo-Aguilar et al., 2005). However, the RTD's tail was not completely captured (Figure 18, panel B), resulting in underestimations of the RTD, this seems to be mainly due to the complex methodology applied when measuring the tracer concentrations at the outlet of the reactor. This result highlighted the relevance of using flow dispersers in BTF operation, not employed in this study to simplify the simulations as the diameter of the dispersers are challenging to mesh and therefore difficult to represent in the simulation.

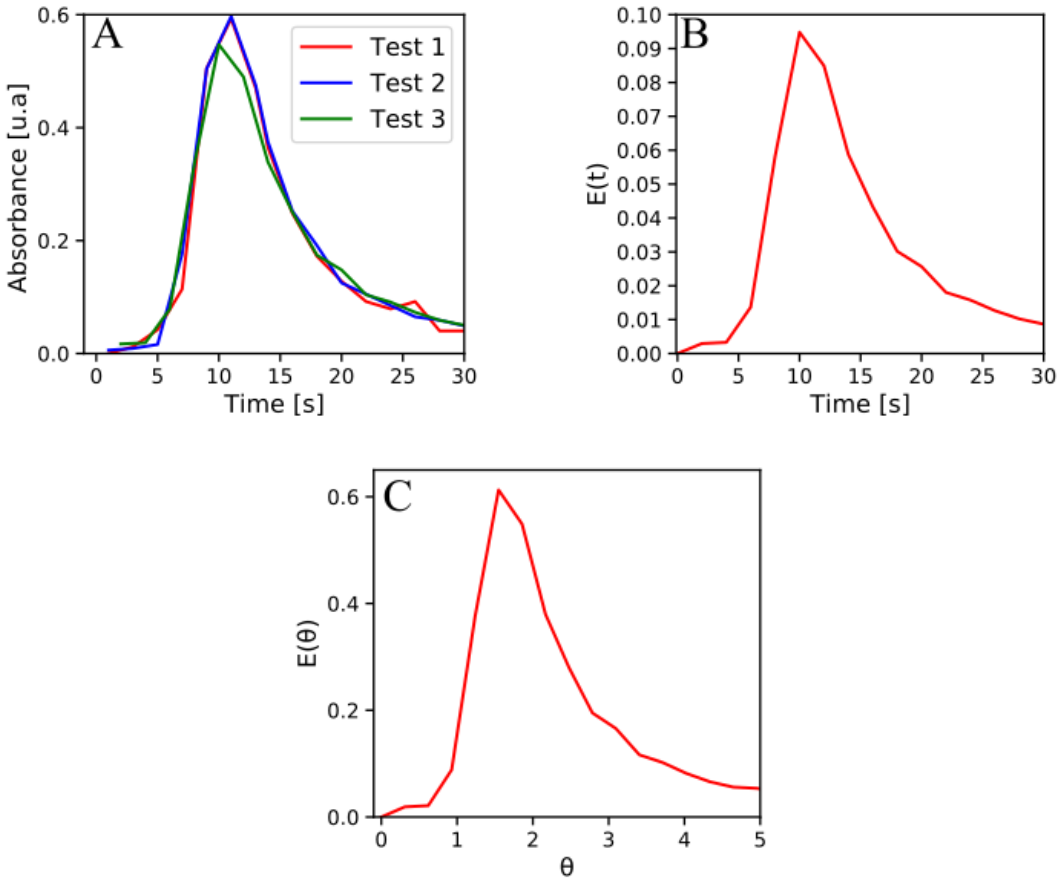

Figure 18. **Liquid phase experimental RTD results.** Time course of the (A) absorbance in triplicate experiments, (B) RTD function, (C) Normalized RTD function.

4.4.2 CFD simulation of the liquid phase

The simulation of the liquid phase was accomplished by applying the same mesh validated for the gas phase and utilizing the same numerical and discretization schemes. As the liquid flow's operational conditions were similar to those of the gas flow, with Reynolds numbers of 552.98 and 6.380 at the inlet and inside the packing structure, respectively, the flow lays within the laminar regime. Hence, the same solvers, used to simulate the gas flow, were used to simulate the liquid flow, to obtain an initial liquid velocity profile to initialize the multiphase (gas-liquid) simulation. The simulation case converged after 1010 iterations. The result of the liquid simulation is shown in Figure 19, where the steady-state velocity magnitudes are depicted in the 3D computational domain. The figure depicts zones of high and low velocities, as the liquid moves through the detailed porous media.

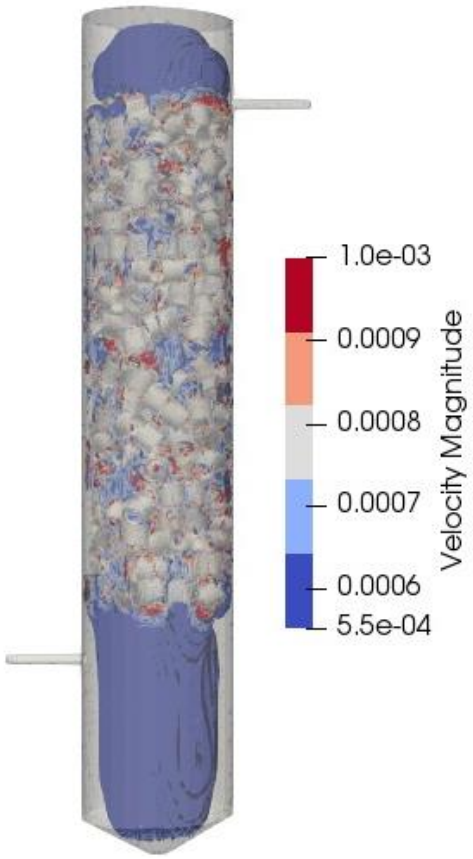

Figure 19. **Steady-state liquid flow velocity magnitude inside the packed bed column**.

4.5 MASS TRANSFER COEFFICIENT DETERMINATION

4.5.1 Experimental volumetric mass transfer coefficient determination

The volumetric mass transfer coefficient obtained, by experimental means, for the oxygen and toluene was 164.6 and 88.3 h^{-1}, respectively. These values agrees with the coefficients reported by Lebrero et al. (2012) of $K_L a_{tol}$ = 95 h^{-1} operating under similar conditions (EBRT = 50 s and TLV = 0.6 m h^{-1}), where the packing material selection causes the rate difference. These results also agree with those reported by Dorado et al. (2008), with a range of $K_L a_{tol}$ between 11-415 h^{-1} using Dixon rings at the same TLV of 2 m h^{-1} and EBRT between 6 and 100 s.

4.5.2 CFD simulation of the mass transfer coefficient

The main objective of this simulation was to obtain the specific surface area available where the oxygen mass transfer occurs. The validation was carried out by applying the volumetric mass transfer coefficient of oxygen into water obtained in Section 4.5.1. This allows the computation of the gas-liquid interphase area and from there the computation of the mass transfer coefficient using the boundary layer theory. The main drawback of multiphase simulations is the expensive computational costs required to reach steady-state conditions. This simulation involved 63 days of continuous computational effort to simulate one real second of operation under a maximum Courant number of 1, which is the condition that defines the stability of the simulation. Thus, the simulation must be initialized from values near the steady-state condition to reduce the computational time. This initial condition was achieved using the internal mesh values at steady state obtained from the gas and liquid simulations performed as explained in the previous sections using the same mesh. As the gas phase model was validated, it is expected that the internal field values for pressure and velocity are reliable. Due to computational costs, the liquid phase simulation was not validated with the RTD since it requires the use of multiphase models at steady state to reproduce this behavior as the liquid phase was not uniformly distributed uniformly inside the internal field. Then, to speed up the process, the velocity vector field of the complete internal mesh at steady state was extracted and mapped from the gas phase simulation, into the multiphase simulation as an initial condition. Later, from the liquid phase simulation, the velocity vector field of the internal mesh was filtered, using the threshold utility from Paraview, in the velocity range between 0.00055 and 0.01 m s^{-1}. The objective of the application of this technique is to try to predict the zones (cells) where the water velocity was above the average. Therefore, we assume that the cells with velocity values above the average are selected to be initialized as water phase ($\alpha = 1$) (Figure 20), as a way to speed up the process of reaching a steady-state condition. Also, the assumption that the liquid phase overlapped the gas phase due to the higher density of the liquid than the gas is applied. This initialization methodology allows the reproduction of a pseudo-steady state condition with values obtained and validated from previous single phase, and less expensive simulations. However, it should be stressed that, with more time availability it is suggested to simulate an extended multiphase simulation until the steady state is reached, which due to time constraint limitations was not an option for the present study. The accelerated approach applied, required a computation time of 6.3 days, to simulate 0.124 s of real-time operation.

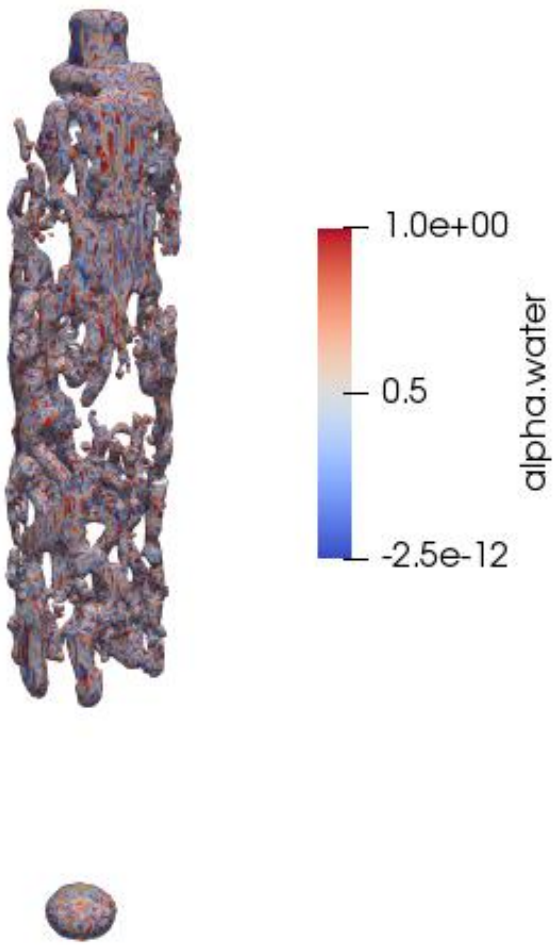

Figure 20. **Gas-Liquid interphase obtained from the multiphase simulation after 0.124 seconds.**

The boundary and initial conditions were the same used in the gas and liquid simulations (Appendix A4). The gas-liquid interphase was extracted by applying a contour filter of the cell values with $\alpha = 0.5$ (Fig 21, panel A). Next, the measurement of local boundary layer thickness was computed in 2D as way to reduce the computational effort. The methodology was similar to that mentioned in Moreno-Casas et al. (2020). First, the interphase's location, length, and area were extracted from the cell data. Secondly, the distance from the interphase and the location where constant air velocity is reached are used to compute the boundary layer thickness, and the average air-free stream velocity (Figure 21, panel B). Then the average K_L value is calculated. Finally, the interphase area is computed by integrating the cell values to obtain the interphase superficial area, value that is later divided by the fluid domain ($5.82 \cdot 10^{-3}\ m^3$) to obtain the parameter a. The obtained values, over the entire reactor,

are then averaged, yielding 0.454 m h^{-1} and 99.845 m^{-1} for for K_L and a, respectively. From here the average values for $K_L a_{O_2} = 45.306$ h^{-1} and $K_L a_{tol} = 24.299$ h^{-1} are calculated using the Eq 28. The discrepancies between $K_L a_{O_2}$ and $K_L a_{tol}$ can be mainly explained by the short simulation time of 0.124 s, which does not match the interphase area that should appear at a steady-state condition. The average value of K_L of 0.454 m h^{-1} is similar to the 0.567 m h^{-1} reported by Moreno-Casas et al. (2020) operating at a TLV = 2 m h^{-1} and EBRT = 60 s. It seems reasonable to expect that running longer computation times may improve simulation results, yielding values of the numerical mass transfer coefficient closer to those the estimated in the experiments.

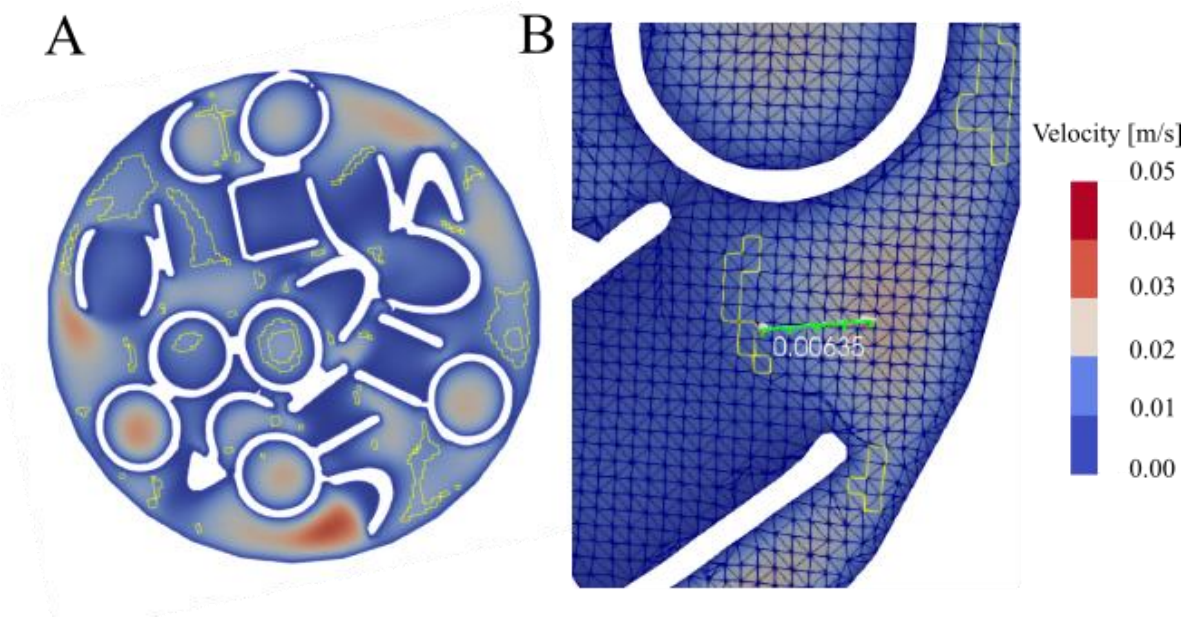

Figure 21. **Boundary layer thickness and air-free surface velocity determination**. (A) Axial view (B) Sagittal view. The cells holding the interphase are represented in yellow. The green lines depict the distance from the cells containing the gas-liquid interphase ($\alpha = 0.5$) to the zones of constant velocity, as a way to compute the boundary layer.

4.6 BIOFILM IMAGING

4.6.1 ASSESSMENT OF THE STEADY STATE AND MAXIMUM ELIMINATION CAPACITY.

The steady-state operation of the BTF at constant a EBRT and TLV was assumed after a

continuous operation of 71 days (Figure 22, panel A). The steady state was assumed when the mean concentration measurements of the EC did not change between two consecutive days of sampling (Figure 22, panel A). The loading rates of 160.91, 198.48, 216.68, 236.21, and 259.34 g m^{-3} h^{-1} were used to estimate the maximum elimination capacity. The EC_{max} obtained in the experiments was 37.321 ± 4.855 g m^{-3} h^{-1} and under this condition the system was not limited by the mass transfer, and the biofilm present inside the packing bed is representative of the maximum capacity. Figure 23 shows the biotrickling filter under these conditions.

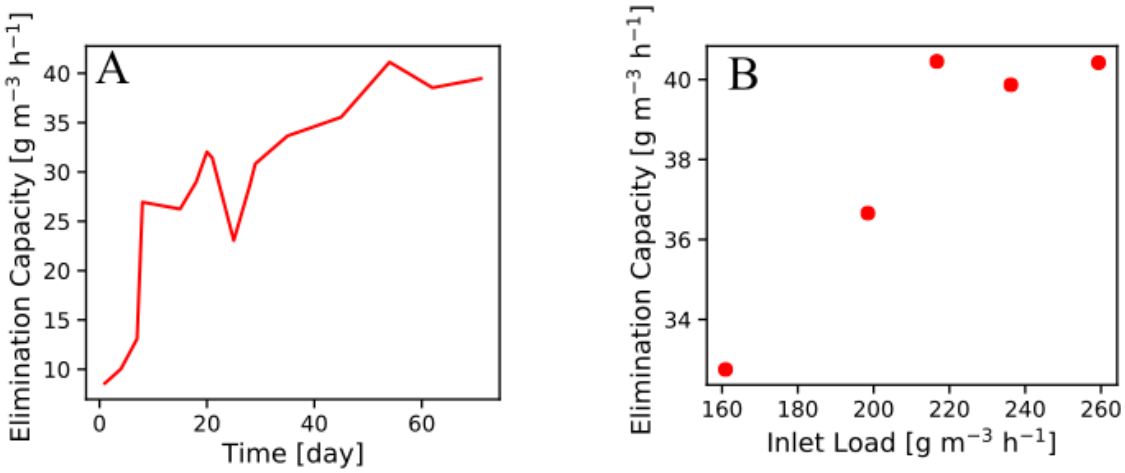

Figure 22: **Steady-state estimation of the biotrickling filter.** (A) Performance of start-up (B) Determination of the maximum elimination capacity.

Figure 23. **Biotrickling filter under maximum elimination capacity**.

4.6.2 BIOFILM IMAGE RECONSTRUCTION

A CT scan of the Biotrickling filter under operation was then obtained. Figure 24 shows the 3D representation of the biotrickling filter reconstructed from a sequence of 1521 2D images in DICOM format obtained from the CT scan.

Figure 24. **Raw computational tomography obtained using contrast agent.**

The results were similar to those obtained in the first tomography, but with a different angle inside the scanner with respect to the vertical axis of the reactor generated complications when trying to emutale the spatial discretization of the abotic CT image described in the section 4.2.1. (Figure 25, panel A).

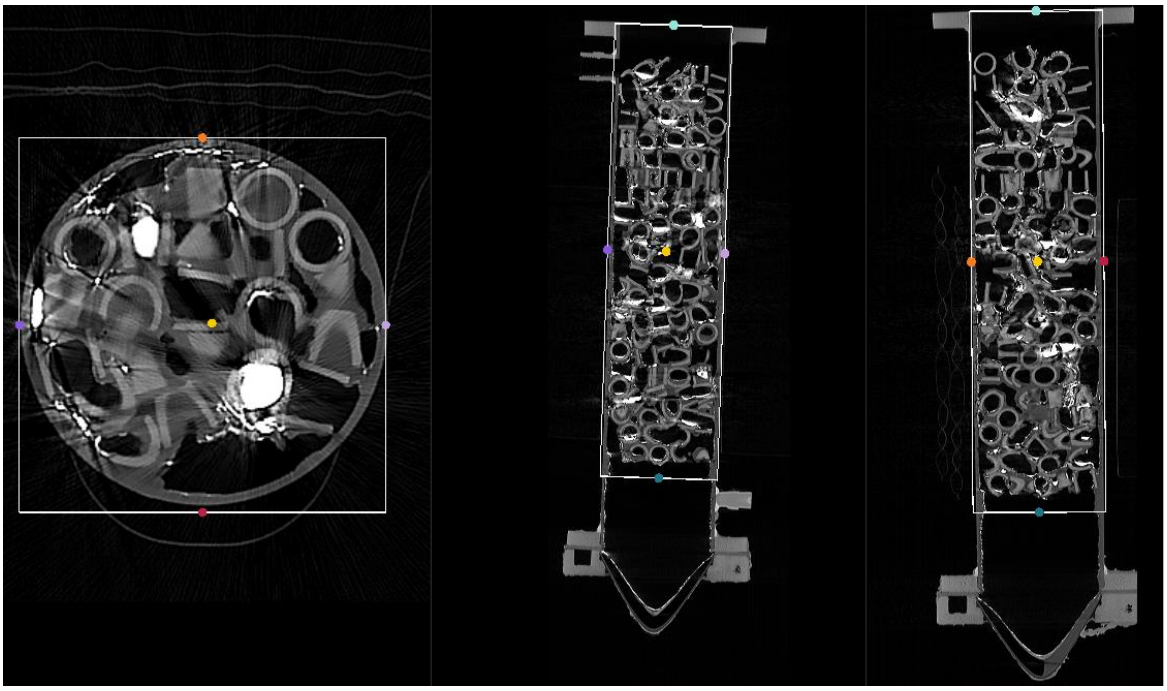

Figure 25. **Axial, coronal, and sagittal slice orientation of the CT with contrast agent.**

The same methodology was applied for the first tomography but with different thresholds. The air was filtered from the image by masking the threshold range between -2957.10 and -500, the biofilm was segmented between -200 and 300, the porous structure was segmented between 500 to 1500, and the contrast between 1500 and 4800. The contrast agent was used to separate the biofilm from the water, as the $BaSO_4$ is insoluble in the biofilm. The main difficulty of the application of the methodology at this stage of the reactor operation was the high accumulation of $BaSO_4$ in some porous zones inside the column, which led to image distortions and reconstruction problems. Yet, the contrast application and analysis seem to be a good approach to studying the dead zones inside packing materials, although further analysis of its usage is out of the scope of this work. Another difficulty found during this process was the similarity in the intensity range between the walls and the biofilm, which led

to difficulties in the segmentation (Figure 26). This segmentation problems were mainly caused by the high computational demand required from the graphic card between the evaluation at different thresholds which limited better reconstructions of the image.

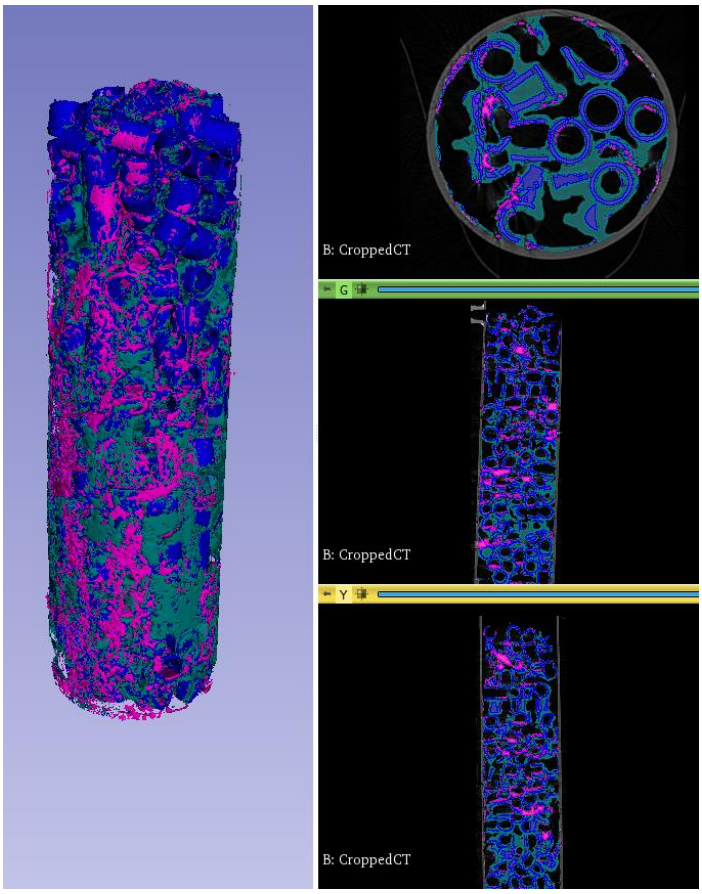

Figure 26. (left image) **3D view of the segmented biofilm**. (right image, from top to bottom) Axial, coronal, and sagittal slice orientation.

In order to simplify the analysis and image reconstruction, the complete internal field (packing material, biofilm, and wetted area) was merged in one segmentation and separated from the walls to be extracted and post-processed as one defined structure (Figure 27).

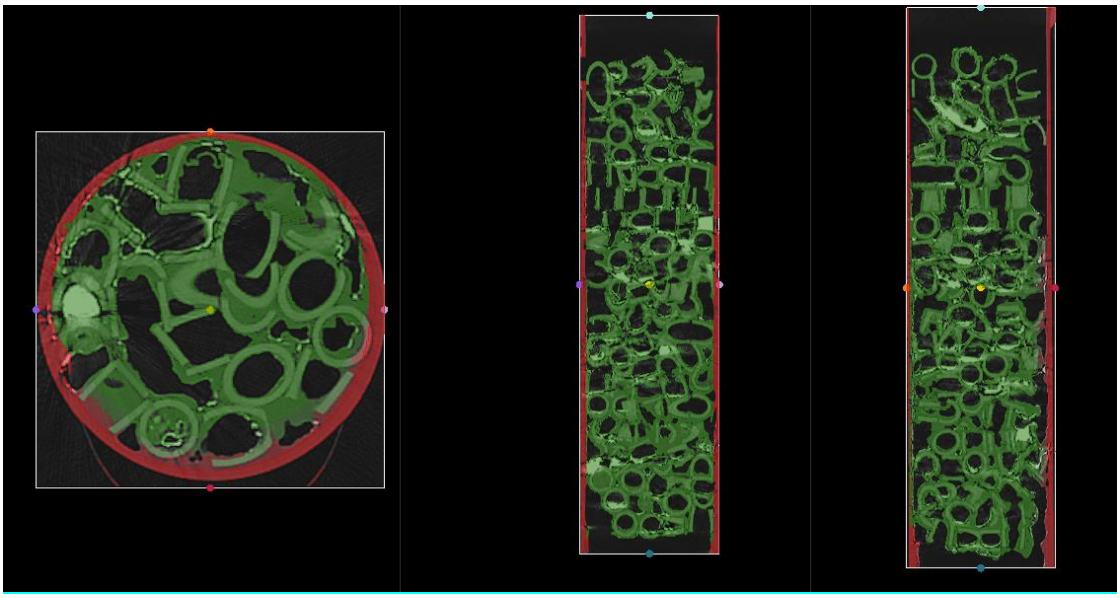

Figure 27. **From left to right: axial, coronal, and sagittal slice orientation of the segmented biofilm over the packing material.**

This structure was merged and centered to match the first CT image of the porous media, that had no biomass growth, to assess the local biofilm formation over the packing material (Figure 28). From the image analysis, the surface area was computed, where it was found that the available surface of the packing material increased from 0.801 m^2, from the case with now biomass, to 1.167 m^2, for the case where biomass grew over the packed bed after operation. This results in 0.366 m^2 of surface which can be computational used as active surface for the biodegradation. In the analysis a finite element mesh is generated that follows the complex geometry of the surfaces composed by the rings and the biofilm. A difficulty of the previous is the computational effort required to separate the biofilm from the ring structure. Mainly because of the complex biofilm geometry, generating mesh errors and uncertainties that required mesh healing techniques to repair and correct the errors found in the geometrical structure. The presence of non-manifold surfaces, identified as free edges of the finite elements representing the composed geometry, did not allow to perform of boolean operations that separated the biofilm from the ring structure (Landier, 2017). Therefore, t-Joints detection and Nodal merging algorithms were applied after the decimation algorithm was used to heal the mesh. As the mesh deviation from the original model is bounded by the mesh element size, the accuracy of the analysis is not affected by the healing process (Chong et al., 2007). However, the expensive computational cost of this algorithm and the angle of

the tomography difficulted the image processing, and additional transforms are required to obtain the biofilm in STL format to perform simulations.

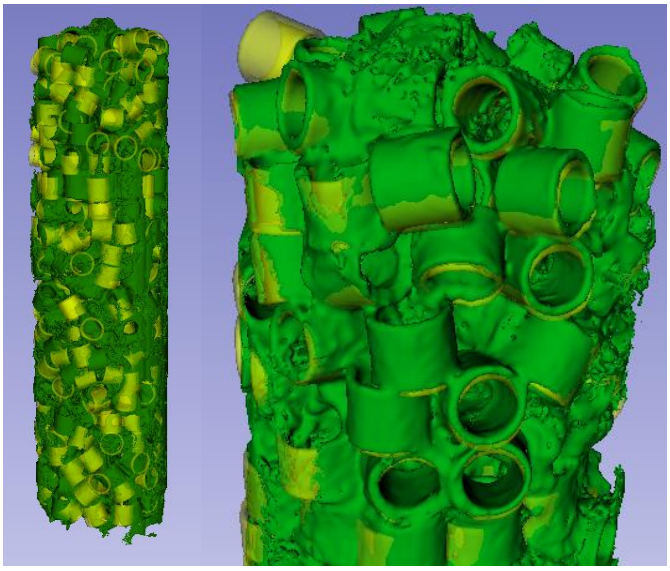

Figure 28. **Biofilm reconstruction over the packing material.** In green the biofilm can be observed, while in yellow the ring packing structure is depicted.

5 CONCLUSIONS

A methodology for validating the gas flow distribution computed by CFD simulations with experimental results using a low-cost MOx sensor has been presented. Additionally, the implementation of an imaging methodology of the biofilm reconstruction over a packing material inside a biotrickling filter was achieved. The proposed methodology was able to predict the RTD of a gas tracer injected experimentally and numerically. Furthermore, the methodology generated the RTD from the CFD simulation, which can be compared with experimental RTD measurements. Later, it was proved that the numerical RTD obtained from CFD was congruent with the experimental RTD. Thus, it could be assumed that the CFD simulation was reliable and used to analyze the flow inside the complex porous matrix, which cannot be done experimentally. The gas phase RTD analysis using a MOx sensor coupled with the CT-CFD simulation was confirmed as an inexpensive methodology to validate the gas flow simulation. The RTD shape and moments were accurately estimated from the simulations and the experimental data and agreed with what has been reported in the

literature. Additional computational time is required to perform the liquid phase RTD and the steady state behavior of the multiphase simulations. However, the current approximations showed the methodology's potential as it yields results similar to experimental and simulation results found in the literature. Additional studies of the contrast imaging methodology are required to improve the knowledge about the contrast concentration influence over image recovery. The use of potassium iodide is suggested in future studies as a contrast agent, as it should improve the intensity difference between the reactor walls and the biofilm, facilitating the segmentation analysis.

Further analysis considering biofilm's abrasion and shear detachment due to contrast agent application must be investigated to improve the local biofilm detection. In addition, high computational capacity is required to post-process the biofilm structure, which opens the doors to investigate or generate new techniques that incur in less expensive computational efforts. The study shows a significant increase in surface area available for mass transfer, however, in the future, separation between the active and nonactive surface available for degradation should be tackle.

The validation procedure presented herein, which helps to validate the prediction capability of the flow dynamics of the CFD-CT simulations, opens the door to analyse in detail the behavior of existing packing beds, contributing to the understanding of the mechanics of the process undergoing inside biotricking filters, at the microscale. Analysis of new packings, performance-oriented optimizations of old packings, or even the computational generated packings that could be printed, is an option that is available at lower costs, to later find suitable options to perform pilots' tests in the lab and validate the advantages of the proposed designs.

Finally, the potential to study the behavior of biomass growth at different operational stages, with different packing configurations, at different gas and liquid flows, becomes a reality. The procedure proposed herein, might allow for the detail study of the correlation of biomass growth and operational configurations, in order to have better insight of the effects of packing and flow conditions, as a way to improve the treatment efficiency of biotrickling filters.

5.1. Future directions

The methodology presented in this study effectively validated the gas flow inside a packed bed reactor. In addition, it delivered insights about implementing 3D biofilm morphologies visualization inside porous media and their implementation in CFD simulations.

The first direction is to run the multiphase simulation in a cluster for about 20 seconds to properly validate the mass transfer determination. Additionally, the Open Source software ImageJ focused on biological image analysis, will be applied to improve the rendering time required to recover the biofilm image. The improvements and more extended simulations may result in applications addressing the interplay between biofilms, local hydrodynamic and mass transport processes in realistic porous media models. With further improvements, this technique would quantify and visualize biofilms in 3D and allow using the mesh cell information to apply biodegradation models in laboratory-scale reactors over validated gas phase RTD. This could improve understanding of the influence of gas flow patterns over pollutant degradation.

Future improvements could also include 3D printing support material's influence over biofilm formation, the study of different gas-liquid flow patterns over the biofilm attachment, and the influence of the contrast concentration over the biofilm visualization.

REFERENCES

Alonso, C., Suidan, M. T., Kim, B. R., & Kim, B. J. (1998a). Dynamic mathematical model for the diodegradation of VOCs in a biofilter: Biomass accumulation study. *Environmental Science and Technology*, *32*(20), 3118–3123. https://doi.org/10.1021/es9711021

Alonso, C., Suidan, M. T., Kim, B. R., & Kim, B. J. (1998b). Dynamic Mathematical Model for the Biodegradation of VOCs in a Biofilter: Biomass Accumulation Study. *Environmental Science & Technology*, *32*(20), 3118–3123. https://doi.org/10.1021/es9711021

Amani, A., Jalilnejad, E., & Mousavi, S. M. (2018). Simulation of phenol biodegradation by Ralstonia eutropha in a packed-bed bioreactor with batch recycle mode using CFD technique. *Journal of Industrial and Engineering Chemistry*, *59*, 310–319. https://doi.org/10.1016/j.jiec.2017.10.037

Aparicio-Mauricio, G., Rodríguez, F. A., Pijpers, J. J. H., Cruz-Díaz, M. R., & Rivero, E. P. (2020). CFD modeling of residence time distribution and experimental validation in a redox flow battery using free and porous flow. *Journal of Energy Storage*, *29*(March), 101337. https://doi.org/10.1016/j.est.2020.101337

Baltzis, B. C., Mpanias, C. J., & Bhattacharya, S. (2001). Modeling the removal of VOC mixtures in biotrickling filters. *Biotechnology and Bioengineering*, *72*(4), 389–401. https://doi.org/10.1002/1097-0290(20000220)72:4<389::AID-BIT1001>3.0.CO;2-#

Baquerizo, G., Maestre, J. P., Sakuma, T., Deshusses, M. A., Gamisans, X., Gabriel, D., & Lafuente, J. (2005). A detailed model of a biofilter for ammonia removal: Model parameters analysis and model validation. *Chemical Engineering Journal*, *113*(2–3), 205–214. https://doi.org/10.1016/j.cej.2005.03.003

Bérard, A., Blais, B., & Patience, G. S. (2020). *Experimental methods in chemical engineering: Residence time distribution—RTD*. *September 2019*, 848–867. https://doi.org/10.1002/cjce.23711

Bird, R. B., Stewart, W. E., & Lightfoot, E. N. (2006). Transport Phenomena. In *John Wiley & Sons, Inc*.

Bonilla-Blancas, W., Mora, M., Revah, S., Baeza, J. A., Lafuente, J., Gamisans, X., Gabriel, D., & González-Sánchez, A. (2015). Application of a novel respirometric methodology to characterize mass transfer and activity of H2S-oxidizing biofilms in

biotrickling filter beds. *Biochemical Engineering Journal*, *99*, 24–34. https://doi.org/10.1016/j.bej.2015.02.030

Caicedo, F., Estrada, J. M., Silva, J. P., Muñoz, R., & Lebrero, R. (2018). Effect of packing material configuration and liquid recirculation rate on the performance of a biotrickling filter treating VOCs: Impact of packing material and liquid recirculation rate on biofiltration performance. *Journal of Chemical Technology & Biotechnology*, *93*(8), 2299–2306. https://doi.org/10.1002/jctb.5573

Caizán-Juanarena, L., Krug, J. R., Vergeldt, F. J., Kleijn, J. M., Velders, A. H., Van As, H., & Ter Heijne, A. (2019). 3D biofilm visualization and quantification on granular bioanodes with magnetic resonance imaging. *Water Research*, *167*, 115059. https://doi.org/10.1016/j.watres.2019.115059

Carrel, M., Beltran, M. A., Morales, V. L., Derlon, N., Morgenroth, E., Kaufmann, R., & Holzner, M. (2017). Biofilm imaging in porous media by laboratory X-Ray tomography: Combining a non-destructive contrast agent with propagation-based phase-contrast imaging tools. *PLoS ONE*, *12*(7), 1–18. https://doi.org/10.1371/journal.pone.0180374

Carrel, M., Morales, V. L., Beltran, M. A., Derlon, N., Kaufmann, R., Morgenroth, E., & Holzner, M. (2018). Biofilms in 3D porous media: Delineating the influence of the pore network geometry, flow and mass transfer on biofilm development. *Water Research*, *134*, 280–291. https://doi.org/10.1016/j.watres.2018.01.059

Cheng, Y., He, H., Yang, C., Zeng, G., Li, X., Chen, H., & Yu, G. (2016). Challenges and solutions for biofiltration of hydrophobic volatile organic compounds. *Biotechnology Advances*, *34*(6), 1091–1102. https://doi.org/10.1016/j.biotechadv.2016.06.007

Chong, C. S., Kumar, A. S., & Lee, H. P. (2007). Automatic mesh-healing technique for model repair and finite element model generation. *Finite Elements in Analysis and Design*, 11.

Cooper, C. M., Fernstrom, G. A., & Miller, S. A. (1944). Performance of Agitated Gas-Liquid Contactors. *Industrial & Engineering Chemistry*, *36*(6), 504–509. https://doi.org/10.1021/ie50414a005

Cox, H. H. J., & Deshusses, M. A. (2001). Biotrickling Filters. In C. Kennes & M. C. Veiga (Eds.), *Bioreactors for Waste Gas Treatment* (Vol. 4, pp. 99–131). Springer Netherlands. https://doi.org/10.1007/978-94-017-0930-9_4

Cristian, P., Mark C.M., van L., & Josehp J., H. (2000). Effect of diffusive and convective substrate transport on biofilm structure formation: A two-dimensional modeling study. *Biotechnology and Bioengineering*, *69*(5), 504–515. https://doi.org/10.1002/1097-0290(20000905)69:5<504::AID-BIT5>3.0.CO;2-S

Davit, Y., Iltis, G., Debenest, G., Veran-Tissoires, S., Wildenschild, D., Gerino, M., & Quintard, M. (2011). Imaging biofilm in porous media using X-ray computed microtomography: IMAGING BIOFILM IN POROUS MEDIA USING X-RAY COMPUTED MICROTOMOGRAPHY. *Journal of Microscopy*, *242*(1), 15–25. https://doi.org/10.1111/j.1365-2818.2010.03432.x

Devinny, J. S., & Hodge, D. S. (1995). Formation of Acidic and Toxic intermediates in Overloaded Ethanol Biofilters. *Journal of the Air & Waste Management Association*, *45*(2), 125–131. https://doi.org/10.1080/10473289.1995.10467348

Devinny, J. S., & Ramesh, J. (2005). A phenomenological review of biofilter models. *Chemical Engineering Journal*, *113*(2–3), 187–196. https://doi.org/10.1016/j.cej.2005.03.005

Diks, R. M. M., & Ottengraf, S. P. P. (1991). Verification studies of a simplified model for the removal of dichloromethane from waste gases using a biological trickling filter. *Bioprocess Engineering*, 7.

Dorado, A. D., Lafuente, F. J., Gabriel, D., & Gamisans, X. (2010). A comparative study based on physical characteristics of suitable packing materials in biofiltration. *Environmental Technology*, *31*(2), 193–204. https://doi.org/10.1080/09593330903426687

Dorado, A. D., RodrÃ-guez, G., Ribera, G., Bonsfills, A., Gabriel, D., Lafuente, J., & Gamisans, X. (2009). Evaluation of Mass Transfer Coefficients in Biotrickling Filters: Experimental Determination and Comparison to Correlations. *Chemical Engineering & Technology*, *32*(12), 1941–1950. https://doi.org/10.1002/ceat.200900275

Dorcea, D., Hnatiuc, M., & Lazar, I. (2019). Acquisition and Calibration Interface for Gas Sensors. *2018 IEEE 24th International Symposium for Design and Technology in Electronic Packaging, SIITME 2018 - Proceedings*, 120–123. https://doi.org/10.1109/SIITME.2018.8599253

Dutta, B. K. (2009). Principles of mass transfer and separation processes. *The Canadian Journal of Chemical Engineering*, *87*(5), 818–819. https://doi.org/10.1002/cjce.20228

Eberl, H. J., Picioreanu, C., & Heijnen, J. J. (2000). A three-dimensional numerical study on the correlation of spatial structure, hydrodynamic conditions, and mass transfer and conversion in bio"lms. *Chemical Engineering Science*, 14.

EPA, U. (2022). *Initial List of Hazardous Air Pollutants with Modifications*. https://www.epa.gov/haps/initial-list-hazardous-air-pollutants-modifications

Estrada, J. M., Dudek, A., Muñoz, R., & Quijano, G. (2014). Fundamental study on gas-liquid mass transfer in a biotrickling filter packed with polyurethane foam. *Journal of Chemical Technology & Biotechnology*, *89*(9), 1419–1424. https://doi.org/10.1002/jctb.4226

Ferziger, J. H., & Perić, M. (2002). *Computational Methods for Fluid Dynamics*. Springer Berlin Heidelberg. https://doi.org/10.1007/978-3-642-56026-2

Fogler, H. S. (2006). Distributions of residence times for chemical reactors. *Elements of Chemical Reaction Engineering*, 867–944.

Gao, X., Li, T., Rogers, W. A., Smith, K., Gaston, K., Wiggins, G., & Parks, J. E. (2020). Validation and application of a multiphase CFD model for hydrodynamics, temperature field and RTD simulation in a pilot-scale biomass pyrolysis vapor phase upgrading reactor. *Chemical Engineering Journal*, *388*, 124279. https://doi.org/10.1016/j.cej.2020.124279

Greenshields, C. J. (2022). OpenFOAM user guide. *OpenFOAM Foundation Ltd*, *2.4.0*(3(1)), 239.

Grinias, J. P., Whitfield, J. T., Guetschow, E. D., & Kennedy, R. T. (2016). An inexpensive, open-source USB Arduino data acquisition device for chemical instrumentation. *Journal of Chemical Education*, *93*(7), 1316–1319. https://doi.org/10.1021/acs.jchemed.6b00262

Groenestijn, J. W. van, & Kraakman, N. J. R. (2005). Recent developments in biological waste gas purification in Europe. *Chemical Engineering Journal*, *113*(2–3), 85–91. https://doi.org/10.1016/j.cej.2005.03.007

Guenther, A., Hewitt, C. N., Erickson, D., Fall, R., Geron, C., Graedel, T., Harley, P., Klinger, L., Lerdau, M., Mckay, W. A., Pierce, T., Scholes, B., Steinbrecher, R.,

Tallamraju, R., Taylor, J., & Zimmerman, P. (1995). A global model of natural volatile organic compound emissions. *Journal of Geophysical Research*, *100*(D5), 8873. https://doi.org/10.1029/94JD02950

Gunjal, P. R., Ranade, V. V., & Chaudhari, R. V. (2003). Liquid distribution and RTD in trickle bed reactors: Experiments and CFD simulations. *Canadian Journal of Chemical Engineering*, *81*(3–4), 821–830. https://doi.org/10.1002/cjce.5450810365

Hartmans, S., & Tramper, J. (1991). Dichloromethane removal from waste gases with a trickle-bed bioreactor. *Bioprocess Engineering*, *6*(3), 83–92. https://doi.org/10.1007/BF00369060

Heymes, F., Manno Demoustier, P., Charbit, F., Louis Fanlo, J., & Moulin, P. (2006). Hydrodynamics and mass transfer in a packed column: Case of toluene absorption with a viscous absorbent. *Chemical Engineering Science*, *61*(15), 5094–5106. https://doi.org/10.1016/j.ces.2006.03.037

Hille, A., Neu, T. R., Hempel, D. C., & Horn, H. (2009). Effective diffusivities and mass fluxes in fungal biopellets. *Biotechnology and Bioengineering*, *103*(6), 1202–1213. https://doi.org/10.1002/bit.22351

Hinkelmann, R. (2005). *Efficient numerical methods and information-processing techniques for modeling hydro and environmental systems* (1st ed). Springer.

Juretic, F. (2017). *cfMesh: Advanced meshing tool*. cfmesh.com

Kennes, C., & Thalasso, F. (1998). Review: Waste gas biotreatment technology. *Journal of Chemical Technology & Biotechnology*, *72*(4), 303–319. https://doi.org/10.1002/(SICI)1097-4660(199808)72:4<303::AID-JCTB903>3.0.CO;2-Y

Kennes, C., & Veiga, M. C. (Eds.). (2001). *Bioreactors for Waste Gas Treatment* (Vol. 4). Springer Netherlands. https://doi.org/10.1007/978-94-017-0930-9

Kennes, C., & Veiga, M. C. (2013). Biotrickling Filters. In C. Kennes & M. C. Veiga (Eds.), *Air Pollution Prevention and Control* (pp. 121–138). John Wiley & Sons, Ltd. https://doi.org/10.1002/9781118523360.ch5

Kensy, F., Zimmermann, H. F., Knabben, I., Anderlei, T., Trauthwein, H., Dingerdissen, U., & Büchs, J. (2005). Oxygen transfer phenomena in 48-well microtiter plates: Determination by optical monitoring of sulfite oxidation and verification by real-time

measurement during microbial growth. *Biotechnology and Bioengineering*, *89*(6), 698–708. https://doi.org/10.1002/bit.20373

Khan, F. I., & Kr. Ghoshal, A. (2000). Removal of Volatile Organic Compounds from polluted air. *Journal of Loss Prevention in the Process Industries*, *13*(6), 527–545. https://doi.org/10.1016/S0950-4230(00)00007-3

Kibazohi, O., Yun, S. Il, & Anderson, W. A. (2004). Removal of hexane in biofilters packed with perlite and a peat-perlite mixture. *World Journal of Microbiology and Biotechnology*, *20*(4), 337–343. https://doi.org/10.1023/B:WIBI.0000033054.15023.71

Kim, S., & Deshusses, M. A. (2003). Development and experimental validation of a conceptual model for biotrickling filtration of H2S. *Environmental Progress*, *22*(2), 119–128. https://doi.org/10.1002/ep.670220214

Kim, S., & Deshusses, M. A. (2008a). Determination of mass transfer coefficients for packing materials used in biofilters and biotrickling filters for air pollution control. 1: Experimental results. *Chemical Engineering Science*, *63*(4), 841–855. https://doi.org/10.1016/j.ces.2007.10.011

Kim, S., & Deshusses, M. A. (2008b). Determination of mass transfer coefficients for packing materials used in biofilters and biotrickling filters for air pollution control 2: Development of mass transfer coefficients correlations. *Chemical Engineering Science*, *63*(4), 856–861. https://doi.org/10.1016/j.ces.2007.10.021

Kirchner, K., & Wagner, S. (1992). Exhaust gas purification using biocatalysts (fixed bacteria monocultures)—The influence of biofilm diffusion rate (02) on the overall reaction rate. *Applied Microbiology and Biotechnology*, *37*(2), 3.

Koch, A. L. (1990). Diffusion The Crucial Process in Many Aspects of the Biology of Bacteria. In K. C. Marshall (Ed.), *Advances in Microbial Ecology* (Vol. 11, pp. 37–70). Springer US. https://doi.org/10.1007/978-1-4684-7612-5_2

Koppmann, R. (Ed.). (2007). *Volatile organic compounds in the atmosphere* (1st ed). Blackwell Pub.

Kraakman, N. J. R., Rocha-Rios, J., & Van Loosdrecht, M. C. M. (2011). Review of mass transfer aspects for biological gas treatment. *Applied Microbiology and Biotechnology*, *91*(4), 873–886. https://doi.org/10.1007/s00253-011-3365-5

Landier, S. (2017). Boolean operations on arbitrary polygonal and polyhedral meshes. *Computer-Aided Design*, *85*, 138–153. https://doi.org/10.1016/j.cad.2016.07.013

Lebrero, R., Estrada, J. M., Muñoz, R., & Quijano, G. (2012). Toluene mass transfer characterization in a biotrickling filter. *Biochemical Engineering Journal*, *60*, 44–49. https://doi.org/10.1016/j.bej.2011.09.017

Lebrero, R., Rodríguez, E., Estrada, J. M., García-Encina, P. A., & Muñoz, R. (2012). Odor abatement in biotrickling filters: Effect of the EBRT on methyl mercaptan and hydrophobic VOCs removal. *Bioresource Technology*, *109*, 38–45. https://doi.org/10.1016/j.biortech.2012.01.052

Lee, S.-H., Li, C., Heber, A. J., & Zheng, C. (2010). Ethylene removal using biotrickling filters: Part I. Experimental description. *Chemical Engineering Journal*, *158*(2), 79–88. https://doi.org/10.1016/j.cej.2009.12.033

Lith, C. van, Leson, G., & Michelsen, R. (1997). Evaluating Design Options for Biofilters. *Journal of the Air & Waste Management Association*, *47*(1), 37–48. https://doi.org/10.1080/10473289.1997.10464410

Lo, Y. M., Hsu, C. H., Yang, S. T., & Min, D. B. (2001). Oxygen transfer characteristics of a centrifugal, packed-bed reactor during viscous xanthan fermentation. *Bioprocess and Biosystems Engineering*, *24*(3), 187–193. https://doi.org/10.1007/s004490100250

Manafpour, M., & Ebrahimnezhadian, H. (2017). *The Multiphase Capability of OpenFoam CFD Toolbox in Solving Flow Field in Hydraulic Structure*. Long-Term Behaviour and Environmentally Friendly Rehabilitation Technologies of Dams (LTBD 2017), Tehran. https://doi.org/10.3217/978-3-85125-564-5-045

Mannucci, A., Munz, G., Mori, G., & Lubello, C. (2012). Biomass accumulation modelling in a highly loaded biotrickling filter for hydrogen sulphide removal. *Chemosphere*, *88*(6), 712–717. https://doi.org/10.1016/j.chemosphere.2012.04.026

Martinez, Burgués, & Marco. (2019a). Fast Measurements with MOX Sensors: A Least-Squares Approach to Blind Deconvolution. *Sensors*, *19*(18), 4029. https://doi.org/10.3390/s19184029

Martinez, D., Burgués, J., & Marco, S. (2019b). Fast measurements with MOX sensors: A least-squares approach to blind deconvolution. *Sensors (Switzerland)*, *19*(18), 1–16. https://doi.org/10.3390/s19184029

Mirabolghasemi, M., Prodanović, M., DiCarlo, D., & Ji, H. (2015). Prediction of empirical properties using direct pore-scale simulation of straining through 3D microtomography images of porous media. *Journal of Hydrology*, *529*, 768–778. https://doi.org/10.1016/j.jhydrol.2015.08.016

Moghaddam, E. M., Foumeny, E. A., Stankiewicz, A. I., & Padding, J. T. (2020). Hydrodynamics of Narrow-Tube Fixed Bed Reactors Filled with Raschig Rings Chemical Engineering Science: X Hydrodynamics of narrow-tube fixed bed reactors filled with Raschig rings. *Chemical Engineering Science: X*, *5*(March), 100057. https://doi.org/10.1016/j.cesx.2020.100057

Mohamadi-Baghmolaei, M., Azin, R., Osfouri, S., & Zendehboudi, S. (2019). Evaluation of mass transfer coefficient for gas condensates in porous systems: Experimental and modeling. *Fuel*, *255*. https://doi.org/10.1016/j.fuel.2019.05.090

Monroy, J. G., Gonźalez-Jimńenez, J., & Blanco, J. L. (2012). Overcoming the slow recovery of MOX gas sensors through a system modeling approach. *Sensors (Switzerland)*, *12*(10), 13664–13680. https://doi.org/10.3390/s121013664

Moreno-Casas, P. A., Scott, F., Delpiano, J., Abell, J. A., Caicedo, F., Muñoz, R., & Vergara-Fernández, A. (2020). Mechanistic Description of Convective Gas-Liquid Mass Transfer in Biotrickling Filters Using CFD Modeling. *Environmental Science & Technology*, *54*(1), 419–426. https://doi.org/10.1021/acs.est.9b02662

Moreno-Casas, P. A., Scott, F., Delpiano, J., & Vergara-Fernández, A. (2020). Computational tomography and CFD simulation of a biofilter treating a toluene, formaldehyde and benzo[α]pyrene vapor mixture. *Chemosphere*, *240*. https://doi.org/10.1016/j.chemosphere.2019.124924

Muñoz, R., Soto, C., Zuñiga, C., & Revah, S. (2018). A systematic comparison of two empirical gas-liquid mass transfer determination methodologies to characterize methane biodegradation in stirred tank bioreactors. *Journal of Environmental Management*, *217*, 247–252. https://doi.org/10.1016/j.jenvman.2018.03.097

Nauman, E. B. (2008). Residence Time Theory. *Industrial & Engineering Chemistry Research*, *47*(10), 3752–3766. https://doi.org/doi: 10.1021/ie071635a

Nieves-Remacha, M. J., Kulkarni, A. A., & Jensen, K. F. (2015). OpenFOAM Computational Fluid Dynamic Simulations of Single-Phase Flows in an Advanced-Flow Reactor.

Industrial & Engineering Chemistry Research, *54*(30), 7543–7553. https://doi.org/10.1021/acs.iecr.5b00232

Ogata, K. (2010). Modern Control Engineering. In M. J. Horton (Ed.), *Prentice Hall* (5th ed.).

Ordaz, A., Ramirez, R., Hernandez-Martinez, G. R., Carrión, M., & Thalasso, F. (2019). Characterization of kinetic parameters and mass transfer resistance in an aerobic fixed-bed reactor by in-situ respirometry. *Biochemical Engineering Journal*, *146*(January), 194–202. https://doi.org/10.1016/j.bej.2019.03.024

Otsu, N. (1979). A Threshold Selection Method from Gray-Level Histograms. *IEEE Transactions on Systems, Man, and Cybernetics*, *9*(1), 62–66. https://doi.org/10.1109/TSMC.1979.4310076

Pascual, C., Cantera, S., Muñoz, R., & Lebrero, R. (2021). Siloxanes removal in a two-phase partitioning biotrickling filter: Influence of the EBRT and the organic phase. *Renewable Energy*, *177*, 52–60. https://doi.org/10.1016/j.renene.2021.05.144

Pedersen, A. R., & Arvin, E. (1995). Removal of toluene in waste gases using a biological trickling filter. *Biodegradation*, *6*(2), 109–118. https://doi.org/10.1007/BF00695341

Poling, B. E., Prausnitz, J. M., & O'Connell, J. P. (2004). The properties of gases and liquids. In *McGraw-Hill* (5th ed., Vol. 5).

Prades, L., Dorado, A. D., Climent, J., Guimerà, X., Chiva, S., & Gamisans, X. (2017). CFD modeling of a fixed-bed biofilm reactor coupling hydrodynamics and biokinetics. *Chemical Engineering Journal*, *313*, 680–692. https://doi.org/10.1016/j.cej.2016.12.107

Prenafeta-Boldú, F. X., Illa, J., Van Groenestijn, J. W., & Flotats, X. (2008). Influence of synthetic packing materials on the gas dispersion and biodegradation kinetics in fungal air biofilters. *Applied Microbiology and Biotechnology*, *79*(2), 319–327. https://doi.org/10.1007/s00253-008-1433-2

Quijano, G., Revah, S., Gutiérrez-Rojas, M., Flores-Cotera, L. B., & Thalasso, F. (2009). Oxygen transfer in three-phase airlift and stirred tank reactors using silicone oil as transfer vector. *Process Biochemistry*, *44*(6), 619–624. https://doi.org/10.1016/j.procbio.2009.01.015

Rahul, Mathur, A. K., Bala, S., & Majumder, C. (2012). Modelling and computational fluid dynamic behaviour of a biofilter treating benzene. *Bioresource Technology*, *125*, 200–207. https://doi.org/10.1016/j.biortech.2012.08.134

Rene, E. R., López, M. E., Veiga, M. C., & Kennes, C. (2010). Performance of a fungal monolith bioreactor for the removal of styrene from polluted air. *Bioresource Technology*, *101*(8), 2608–2615. https://doi.org/10.1016/j.biortech.2009.10.060

Revah, S., & Morgan-Sagastume, J. M. (2005). Methods of Odor and VOC Control. In Z. Shareefdeen & A. Singh (Eds.), *Biotechnology for Odor and Air Pollution Control* (pp. 29–63). Springer-Verlag. https://doi.org/10.1007/3-540-27007-8_3

Runye, Z., Christian, K., Zhuowei, C., Lichao, L., Jianming, Y., & Jianmeng, C. (2015). Styrene removal in a biotrickling filter and a combined UV–biotrickling filter: Steady- and transient-state performance and microbial analysis. *Chemical Engineering Journal*, *275*, 168–178. https://doi.org/10.1016/j.cej.2015.04.016

Sadino-Riquelme, C., Hayes, R. E., Jeison, D., & Donoso-Bravo, A. (2018). Computational fluid dynamic (CFD) modelling in anaerobic digestion: General application and recent advances. *Critical Reviews in Environmental Science and Technology*, *48*(1), 39–76. https://doi.org/10.1080/10643389.2018.1440853

San-Valero, P., Dorado, A. D., Martínez-Soria, V., & Gabaldón, C. (2018). Biotrickling filter modeling for styrene abatement. Part 1: Model development, calibration and validation on an industrial scale. *Chemosphere*, *191*, 1066–1074. https://doi.org/10.1016/j.chemosphere.2017.10.069

San-Valero, P., Gabaldón, C., Penya-roja, J., & Pérez, M. C. (2012). Study of Mass Oxygen Transfer in a Biotrickling Filter for Air Pollution Control. *Procedia Engineering*, *42*, 1726–1730. https://doi.org/10.1016/j.proeng.2012.07.565

San-Valero, P., Penya-Roja, J. M., Álvarez-Hornos, F. J., & Gabaldón, C. (2014). Modelling mass transfer properties in a biotrickling filter for the removal of isopropanol. *Chemical Engineering Science*, *108*, 47–56. https://doi.org/10.1016/j.ces.2013.12.033

Schmuker, M., Bahr, V., & Huerta, R. (2016). Exploiting plume structure to decode gas source distance using metal-oxide gas sensors. *Sensors and Actuators, B: Chemical*, *235*, 636–646. https://doi.org/10.1016/j.snb.2016.05.098

Shareefdeen, Z., & Singh, A. (Eds.). (2005). *Biotechnology for odor and air pollution control*. Springer-Verlag.

Sharvelle, S., McLamore, E., & Banks, M. K. (2008). Hydrodynamic characteristics in biotrickling filters as affected by packing material and hydraulic loading rate. *Journal of Environmental Engineering*, *134*(5), 346–352. https://doi.org/10.1061/(ASCE)0733-9372(2008)134:5(346)

Singh, R. K., Wang, C., & Xu, Z. (2018). Residence time distribution in a structured packing unit for monitoring aerosol emissions. *International Journal of Greenhouse Gas Control*, *79*(October), 181–192. https://doi.org/10.1016/j.ijggc.2018.11.001

Soulaine, C., Roman, S., Kovscek, A., & Tchelepi, H. A. (2018). Pore-scale modelling of multiphase reactive flow: Application to mineral dissolution with production of CO2. *Journal of Fluid Mechanics*, *855*, 616–645. https://doi.org/10.1017/jfm.2018.655

Transport phenomena, R. B. Bird, W. E. Stewart, and E. N. Lightfoot, John Wiley and Sons, Inc., New York(1960). 780 pages.$11.50. (1961). *AIChE Journal*, *7*(2), 5J-6J. https://doi.org/10.1002/aic.690070245

Trejo-Aguilar, G., Revah, S., & Lobo-Oehmichen, R. (2005). Hydrodynamic characterization of a trickle bed air biofilter. *Chemical Engineering Journal*, *113*(2–3), 145–152. https://doi.org/10.1016/j.cej.2005.04.001

Vergara-Fernandez, A., Scott, F., Carreno-Lopez, F., Aroca, G., Moreno-Casas, P., Gonzalez-Sanchez, A., & Munoz, R. (2020). A comparative assessment of the performance of fungal-bacterial and fungal biofilters for methane abatement. *Journal of Environmental Chemical Engineering*, *8*(5), 104421. https://doi.org/10.1016/j.jece.2020.104421

Wagner, M., Taherzadeh, D., Haisch, C., & Horn, H. (2010). Investigation of the mesoscale structure and volumetric features of biofilms using optical coherence tomography. *Biotechnology and Bioengineering*, *107*(5), 844–853. https://doi.org/10.1002/bit.22864

Wang, C., Xu, Z., Lai, C., & Sun, X. (2018). Beyond the standard two-film theory: Computational fluid dynamics simulations for carbon dioxide capture in a wetted wall column. *Chemical Engineering Science*, *184*, 103–110. https://doi.org/10.1016/j.ces.2018.03.021

Wang, C., Yin, L., Zhang, L., Xiang, D., & Gao, R. (2010). Metal oxide gas sensors: Sensitivity and influencing factors. *Sensors*, *10*(3), 2088–2106. https://doi.org/10.3390/s100302088

Wang, G. Q., Yuan, X. G., & Yu, K. T. (2005). Review of mass-transfer correlations for packed columns. *Industrial and Engineering Chemistry Research*, *44*(23), 8715–8729. https://doi.org/10.1021/ie050017w

Weller, H. G., Tabor, G., Jasak, H., & Fureby, C. (1998). A tensorial approach to computational continuum mechanics using object-oriented techniques. *Computers in Physics*, *12*(6), 620. https://doi.org/10.1063/1.168744

Wicklein, E., Batstone, D. J., Ducoste, J., Laurent, J., Griborio, A., Wicks, J., Saunders, S., Samstag, R., Potier, O., & Nopens, I. (2016). Good modelling practice in applying computational fluid dynamics for WWTP modelling. *Water Science and Technology*, *73*(5), 969–982. https://doi.org/10.2166/wst.2015.565

World Health Organization. (2018). Health, environment and climate change. Road map for an enhanced global response to the adverse health effects of air pollution. *Seventy-First World Health Assembly, 2016 (April)*, 1–8.

Wu, H., Yan, H., Quan, Y., Zhao, H., Jiang, N., & Yin, C. (2018a). Recent progress and perspectives in biotrickling filters for VOCs and odorous gases treatment. *Journal of Environmental Management*, *222*(May), 409–419. https://doi.org/10.1016/j.jenvman.2018.06.001

Wu, H., Yan, H., Quan, Y., Zhao, H., Jiang, N., & Yin, C. (2018b). Recent progress and perspectives in biotrickling filters for VOCs and odorous gases treatment. *Journal of Environmental Management*, *222*, 409–419. https://doi.org/10.1016/j.jenvman.2018.06.001

Yang, C., Chen, H., Zeng, G., Yu, G., & Luo, S. (2010). Biomass accumulation and control strategies in gas biofiltration. *Biotechnology Advances*, *28*(4), 531–540. https://doi.org/10.1016/j.biotechadv.2010.04.002

Yang, C., Yu, G., Zeng, G., Yang, H., Chen, F., & Jin, C. (2011). Performance of biotrickling filters packed with structured or cubic polyurethane sponges for VOC removal. *Journal of Environmental Sciences*, *23*(8), 1325–1333. https://doi.org/10.1016/S1001-0742(10)60565-7

Yurt, N., Beyenal, H., Sears, J., & Lewandowski, Z. (2003). Quantifying selected growth parameters of Leptothrix discophora SP-6 in biofilms from oxygen concentration profiles. *Chemical Engineering Science*, *58*(20), 4557–4566. https://doi.org/10.1016/S0009-2509(03)00344-0

Zarook, S. M., Shaikh, A. A., & Azam, S. M. (1998). Axial dispersion in biofilters. *Biochemical Engineering Journal*, *1*(1), 77–84. https://doi.org/10.1016/S1369-703X(97)00012-0

Zhu, L., Kolesov, I., Gao, Y., Kikinis, R., & Tannenbaum, A. (2014). *An Effective Interactive Medical Image Segmentation Method Using Fast GrowCut*. 9.

Zhu, X., Suidan, M. T., Pruden, A., Yang, C., Alonso, C., Kim, B. J., & Kim, B. R. (2004). Effect of Substrate Henry's Constant on Biofilter Performance. *Journal of the Air & Waste Management Association*, *54*(4), 409–418. https://doi.org/10.1080/10473289.2004.10470918

APPENDIX

A1. MOX SENSOR CALIBRATION CURVE

Calibration curve equation for iso-butane:

$$C = 10^{-2.1116 \cdot \log\left(\frac{R_S}{R_0}\right) + 2.7412} \text{ with an } R^2 = 0.999 \quad \text{(S1)}.$$

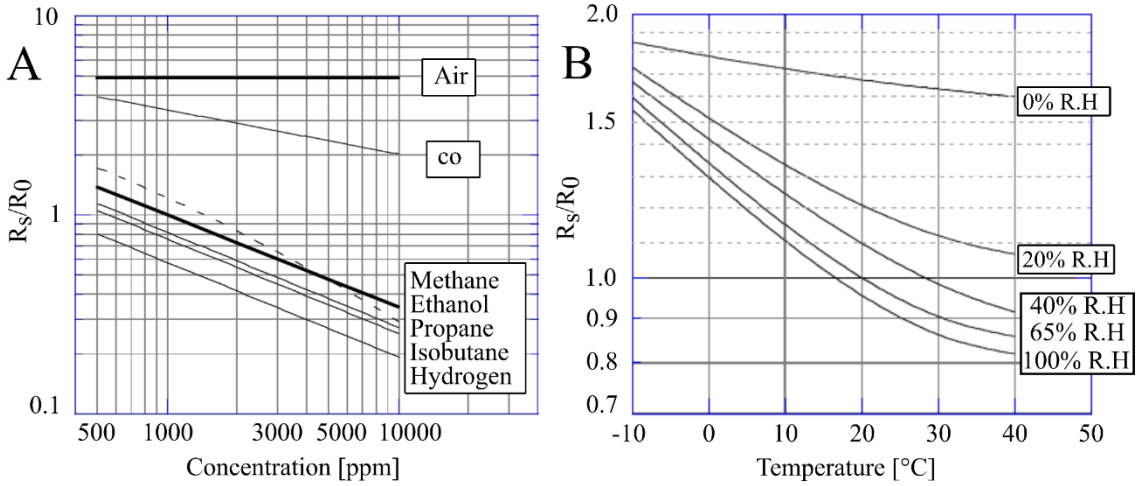

Figure A1. TGS813 sensitivity characteristics. **(A)** Relative sensitivity based on the ratio of the sensor resistance in various gases (R_s) to the sensor resistance in 1000 ppm of methane (R_0). **(B)** Temperature and humidity dependency based on the ratio of the sensor resistance in 1000 ppm of methane under different atmospheric conditions (R_s) to the sensor resistance in 1000 ppm of methane at 20°C and 65% relative humidity (R_0).

A2. CIRCUIT DIAGRAM

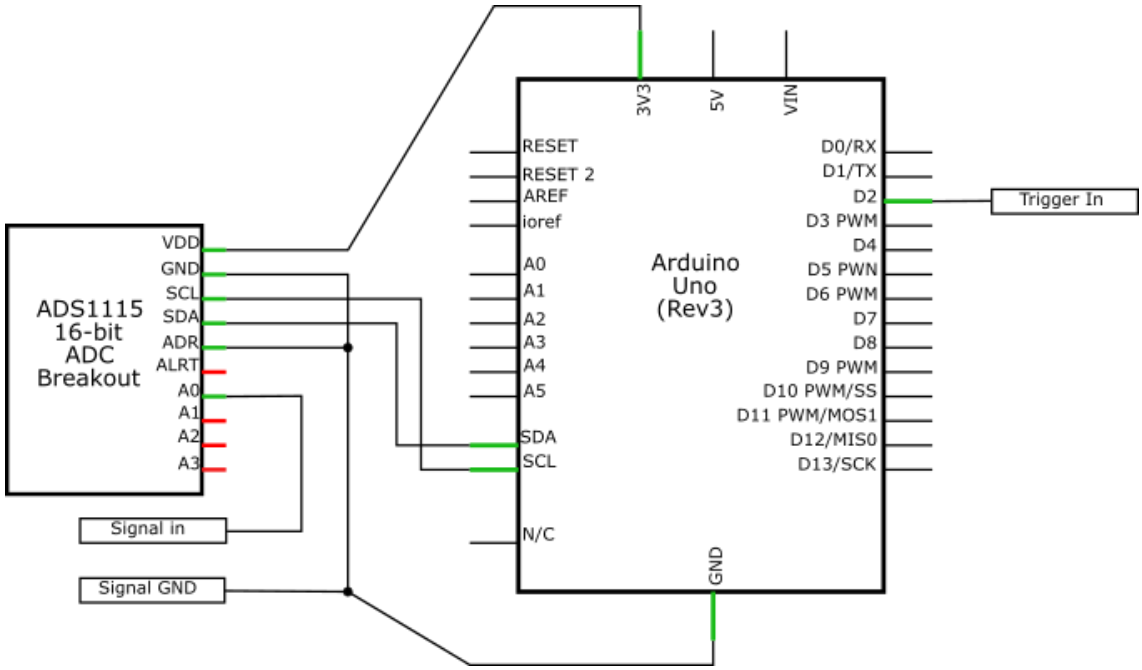

Figure A2. Sensor circuit diagram.

A3. CT SCAN PROPERTIES

For reproducibility, the information from the following tables shows the information of the CT scan and simulation properties.

Table A1: CT Scan properties

Properties	Value
Scan Lenght	760.5 mm
Scan Time	51.32 s
Focal Spot Resolution	STANDARD
Image Type	AXIAL
Collimation	64x0.625 mm
Slice Thickness	1.00 mm
Slice Increment	-0.50 mm
Pitch	0.30
Rotation Time	0.75 s
Field of View	250.00 mm
Voltage	120 kV
Current	118 mA
mAs	297

A4. SIMULATION PROPERTIES

Table A2: Initial and boundary conditions of the SIMPLE simulation.

Region	**Base Type**	$\vec{u}$	P
		Value [m/s]	**Value [Pa]**
Inlet	Patch	(2.653 0 0)	-
Outlet	Patch	-	0
Walls	Wall	-	-
Porous Domain	Wall	-	-

Table A3: Simulation conditions for the RTD simulation.

Region	**Base Type**	T
		Value
Inlet	Patch	1
Outlet	Patch	-
Walls	Wall	-
Porous Doman	Wall	-

Table A4: simpleFOAM fvSchemes and fvSolution parameters used in the CFD simulations.

Type	**Parameter**	**Value**
Time Terms	ddtSchemes	steadyState
Gradient Terms	gradSchemes	default cellMDLimited Gauss linear 0; grad(U) cellMDLimited Gauss linear 0.333;
Convective Terms	divSchemes	div(phi,U) bounded Gauss upwind; div((nuEff*dev2(T(grad(U))))) Gauss linear;
Interpolation Schemes	interpolationSchemes	default linear;
Laplacian Schemes	laplacianSchemes	default Gauss linear limited 0.5;
Surface Normal Gradient Schemes	snGradSchemes	default limited 0.5;
Solvers P	solver preconditioner	PCG; DIC;

	tolerance relTol	1e-04; 0.01;
Solvers U	solver preconditioner tolerance relTol	PBiCGStab; DILU; 1e-08; 0.0;

Table A5: scalarTransportFOAM fvSchemes and fvSolution parameters used in the CFD simulations.

Type	**Parameter**	**Value**
Time Terms	ddtSchemes	default Euler;
Gradient Terms	gradSchemes	default Gauss linear;
Convective Terms	divSchemes	default none; div(phi,T) Gauss linearUpwind grad(T);
Interpolation Schemes	interpolationSchemes	default linear;
Laplacian Schemes	laplacianSchemes	default none; laplacian(DT,T) Gauss linear corrected;
Surface Normal Gradient Schemes	snGradSchemes	default corrected;
Solvers T	solver preconditioner tolerance relTol	PBiCGStab;DIC; DILU; 1e-06; 0;

Table A6: Initial and boundary conditions of the SIMPLE simulation.

Region	**Base Type**	α**.water**	P_rgh	$\vec{u}$
		Value	**Value [Pa]**	**Value [m/s]**
Gas_inlet	Patch	type inletOutlet; inletValue uniform 0; value uniform 0;	type zeroGradient;	type inletOutlet; inletValue uniform (2.656 0 0); value uniform (0 0 0);
Gas_Outlet	Patch	type inletOutlet; inletValue uniform 0;	type fixedVale; Value uniform 0;	type zeroGradient;

		value uniform 0;		
Liquid_Inlet	Patch	type inletOutlet; inletValue uniform 1; value uniform 1;	type zeroGradient;	type inletOutlet; inletValue uniform (0 - 0.00331345 0); value uniform (0 0 0);
Liquid_Outlet	Patch	type inletOutlet; inletValue uniform 1; value uniform 1	type fixedVale; Value uniform 0;	type zeroGradient;
Porous Domain	Wall	type zeroGradient;	type zeroGradient;	type noSlip;
Walls	Wall	type zeroGradient;	type zeroGradient;	type noSlip;

Table A7 interFOAM fvSchemes and fvSolution parameters used in the CFD simulations.

Type	**Parameter**	**Value**
Time Terms	ddtSchemes	default Euler;
Gradient Terms	gradSchemes	default Gauss linear;

Convective Terms	divSchemes	div(rhoPhi,U) Gauss
		linearUpwind grad(U);
		div(phi,alpha) Gauss vanLeer;
		div(phirb,alpha) Gauss linear;
		
		div(((rho*nuEff)*dev2(T(grad(U)))))
		Gauss linear;

Interpolation Schemes	interpolationSchemes	default linear;
Laplacian Schemes	laplacianSchemes	default Gauss linear corrected;
Surface Normal Gradient Schemes	snGradSchemes	default corrected;
Solvers α.water	solver smoother tolerance relTol	smoothSolver;; symGaussSeidel;; 1e-08; 0;
Solvers P_rgh	solver	PCG;

	preconditioner tolerance relTol	DIC; 1e-07; 0.05;
Solvers U	solver smoother tolerance relTol	smoothSolver;; symGaussSeidel;; 1e-06; 0;